

# Global phase diagram of a dirty Weyl semimetal

Bitan Roy,<sup>1,2</sup> Robert-Jan Slager,<sup>3</sup> and Vladimir Jurićć<sup>4</sup>

<sup>1</sup>*Condensed Matter Theory Center and Joint Quantum Institute,  
University of Maryland, College Park, Maryland 20742-4111, USA*

<sup>2</sup>*Department of Physics and Astronomy, Rice University, Houston, Texas 77005, USA*

<sup>3</sup>*Max-Planck-Institut für Physik komplexer Systeme, Nöthnitzer Str. 38, 01187 Dresden, Germany*

<sup>4</sup>*Nordita, Center for Quantum Materials, KTH Royal Institute of Technology  
and Stockholm University, Roslagstullsbacken 23, 10691 Stockholm, Sweden*

(Dated: June 19, 2022)

We here theoretically study the global phase diagram of a three-dimensional dirty Weyl system. The generalized Harris criterion, augmented by a perturbative renormalization-group (RG) analysis shows that weak disorder is an irrelevant perturbation at the Weyl semimetal(WSM)-insulator quantum critical point (QCP). But, a metallic phase sets in through a quantum phase transition (QPT) at strong disorder across a multicritical point, characterized by the correlation length exponent  $\nu = 2$  and dynamic scaling exponent (DSE)  $z = 5/4$ . Deep inside the WSM phase, generic disorder is also an irrelevant perturbation, while a metallic phase appears at strong disorder through a QPT. We here demonstrate that in the presence of generic, but chiral symmetric disorder (e.g., chemical potential, axial potential, etc.) the WSM-metal QPT is always characterized by the exponents  $\nu = 1$  and  $z = 3/2$  to one-loop order. We here anchor such emergent *chiral superuniversality* through complimentary RG calculations, controlled via  $\epsilon$ -expansions, and numerical analysis of average density of states across WSM-metal QPT. Even though in the presence of chiral symmetry breaking disorder, as for instance random spin-orbit coupling, the exact value of DSE across such QPT depends on the RG scheme, we always find  $z > d$ , with  $d$  as dimensionality of the WSM, and  $\nu = 1$ . We also discuss scaling behavior of various physical observables, such as residue of quasiparticle pole, dynamic conductivity, specific heat, Grüneisen ratio, across the WSM-metal QPTs.

## I. INTRODUCTION

The complex energy landscape of electronic quantum-mechanical states in a solid state compound, commonly known as band structure, can often display *band touching* at isolated points in the Brillouin zone, which can be either accidental or symmetry protected [1–9]. In the vicinity of such diabolic points, the low energy excitations can be described as quasi-relativistic Dirac or Weyl fermions [12, 13], which may provide an ideal platform for condensed matter realization of various peculiar phenomena, such as the chiral anomaly, Casimir effect, and axionic electrodynamics [10, 11]. Recently, three dimensional Weyl semimetals (WSMs) have attracted a lot of interest due to the growing evidence of their material realization [14–23]. A WSM, the prime example of a gapless topological phase of matter, is constituted by so called Weyl nodes that in the reciprocal space (Brillouin zone) act as the source and sinks of Abelian Berry curvature, and thus always appear in pairs [24]. In a nutshell, the Abelian Berry flux enclosed by the system determines the integer topological invariant of a WSM and the degeneracy of topologically protected surface Fermi arc. A question of fundamental and practical importance in this context concerns the stability of such gapless topological phase against impurities or disorder, inevitably present in real materials. Combining complementary field theoretic renormalization group (RG) calculations and a numerical analysis of the average density of states (DOS), we here study the role of randomness in various regimes of the phase diagram of a Weyl system to arrive at the *global*

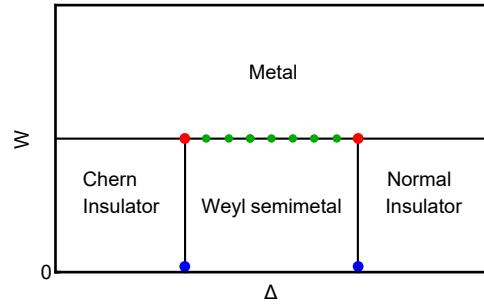


Figure 1: A schematic phase diagram of a dirty Weyl semimetal. Here,  $\Delta$  is a tuning parameter that drives quantum phase transition from Weyl semimetal to (Chern or normal) insulator in clean system, and  $W$  denotes the strength of disorder (the nature of which is not specified here). Semimetal-insulator quantum critical points are denoted by the blue dots. The red dots represent multicritical points, where an insulator, a metal and the Weyl semimetal meet. The string of green dots represents a line of quantum critical points through one of which (depending on the bare value of  $\Delta$ ) the Weyl semimetal undergoes a quantum phase transition into a metallic phase. The shape of the phase boundaries is, however, non-universal.

*phase diagram*, schematically illustrated in Fig. 1.

A WSM can be constructed by appropriately stacking two-dimensional layers of quantum anomalous Hall insulator (QAHI) in the momentum space along the  $k_z$  direction, for example. Thus, by construction a WSM inherits the two dimensional integer topological invariant of constituting layers of QAHI, and the *momentum space*

*skyrmion number* of QAH jumps by an integer amount across two Weyl nodes. As a result, the Weyl nodes serve as the source and sinks for Abelian Berry curvature, and in a clean system WSM is sandwiched between a topological Chern and a trivial insulating phase, as shown in Fig. 1. In an effective tight-binding model a WSM-insulator quantum phase transition (QPT) can be tuned by changing the effective hopping in the  $k_z$  direction, as demonstrated in Sec. II. In this work we first assess the stability of such clean semimetal-insulator quantum critical point (QCP) in the presence of generic randomness in the system. In this regard we come to the following conclusions.

1. By generalizing the Harris criterion [25], we argue that WSM-insulator QCP is *stable* against sufficiently weak, but otherwise generic disorder (see Sec. III). Such an outcome is further substantiated from the scaling analysis of disorder coupling, suggesting that disorder is an *irrelevant* perturbation at such a QCP.
2. Subscribing to an appropriate  $\epsilon$ -expansion (see Sec. III), we demonstrate that a *multicritical* point emerges at stronger disorder, where the WSM, a band insulator (either Chern or trivial) and metallic phases meet. The clean WSM-insulator QCP then becomes unstable toward the formation of a compressible metal. The exponents capturing the instability of critical excitations toward the formation of a metal are: (a) correlation length exponent (CLE)  $\nu = 2$ , and (b) dynamic scaling exponent (DSE)  $z = 5/4$  to the leading order in  $\epsilon$  expansion. These two exponents also determine the scaling behavior of physical observables across the anisotropic critical semimetal-metal QPT.

We now turn our focus onto the WSM phase. The study of disorder effects in topological phases of matter has recently attracted a lot of attention, leading to a surge of analytical [26–47] and numerical [48–61] works. In particular, the focus has been concentrated on massless Dirac critical point separating two topologically distinct insulators (electrical or thermal), as well as inside a Dirac and Weyl semimetal phases. Even though the effects of generic disorders have been studied to some extent theoretically [28, 34, 39–41], most of the numerical works solely focused on random charge impurities (for exception see Refs. [51, 53]). By now there is both analytical and numerical evidence that chemical potential disorder when strong enough drives a QPT from the WSM to a diffusive metal, leaving its imprint on different observables, e.g., average density of states (DOS), specific heat and conductivity. Deep inside the WSM phase, the system possesses various *emergent* symmetries (see Table II), such as a *continuous global chiral  $U(1)$*  symmetry that is tied with the translational symmetry of a clean noninteracting WSM in the continuum limit [62]. In the absence of both inversion and time-reversal symmetries,

the simplest realization of a WSM with only two Weyl nodes is susceptible to *sixteen* possible sources of elastic scattering, displayed in Table II. They can be grouped in *eight* classes, among which only four preserve the emergent global chiral symmetry (intranode scattering), while the remaining ones directly mix two Weyl nodes with opposite (left and right) chiralities. As we demonstrate in the paper such characterization of disorders based on the chiral symmetry allows us to classify the WSM-metal QPTs in the presence of generic disorder.

To motivate our theoretical analysis, we now discuss the possible microscopic origin of disorders in the Weyl materials. Furthermore, knowing this in future may allow a control over randomness in experiments on these materials. For example, chemical potential disorder can be controlled by modifying the concentration of random charge impurities. Random asymmetric shifts of chemical potential between the left and right chiral Weyl cones correspond to the *axial potential disorder*. Therefore, in an inversion asymmetric WSM such disorder is always present. Magnetic disorder is yet another type of chiral symmetry preserving (CSP) disorder, and the strength of random magnetic scatterers can be efficiently tuned by systematically injecting magnetic ions in the system [63]. In contrast, all chiral symmetry breaking (CSB) disorders cause mixing of two Weyl nodes and in an effective model for WSMs they stem from various types of *random bond* disorder. Therefore, strength of CSB disorder may be tuned by applying *inhomogeneous* pressure (hydrostatic or chemical) in the Weyl materials. Since the WSMs are found in strong spin-orbit coupled materials, a random spin-orbit coupling can be achieved when hopping (hybridization) between two orbitals with opposite parity acquires random spatial modulation. Yet another CSB but vector-like type of disorder is a random axial Zeeman coupling. Its source is the different  $g$ -factor of two hybridizing bands that cross at the Weyl point [64–66]. Therefore, when magnetic impurities are injected in the system such disorder is naturally introduced, and depending on the relative strength of the  $g$ -factor in different bands, one can access regular or axial random magnetic coupling. Finally, two different types of CSB *mass* disorders that tend to gap out the Weyl points are represented by random charge- or spin-density-wave order, depending on the microscopic details [67]. These disorders correspond to random scalar and pseudo-scalar mass. Due to their presence, Weyl nodes are gapped out in each disorder configuration, but the sign of the gap is random from realization to realization, and in the thermodynamic limit the nodes remain gapless. To the best of our knowledge, it is currently unknown how to tune the strength of all individual sources of elastic scattering in real Weyl materials. Nevertheless, we elucidate how all possible disorders can be obtained from a simple effective tight-binding model on a cubic lattice for a WSM with two nodes (see Appendix D), allowing us to numerically investigate the effects of generic disorder in a WSM.

Here we address the stability of a disordered WSM

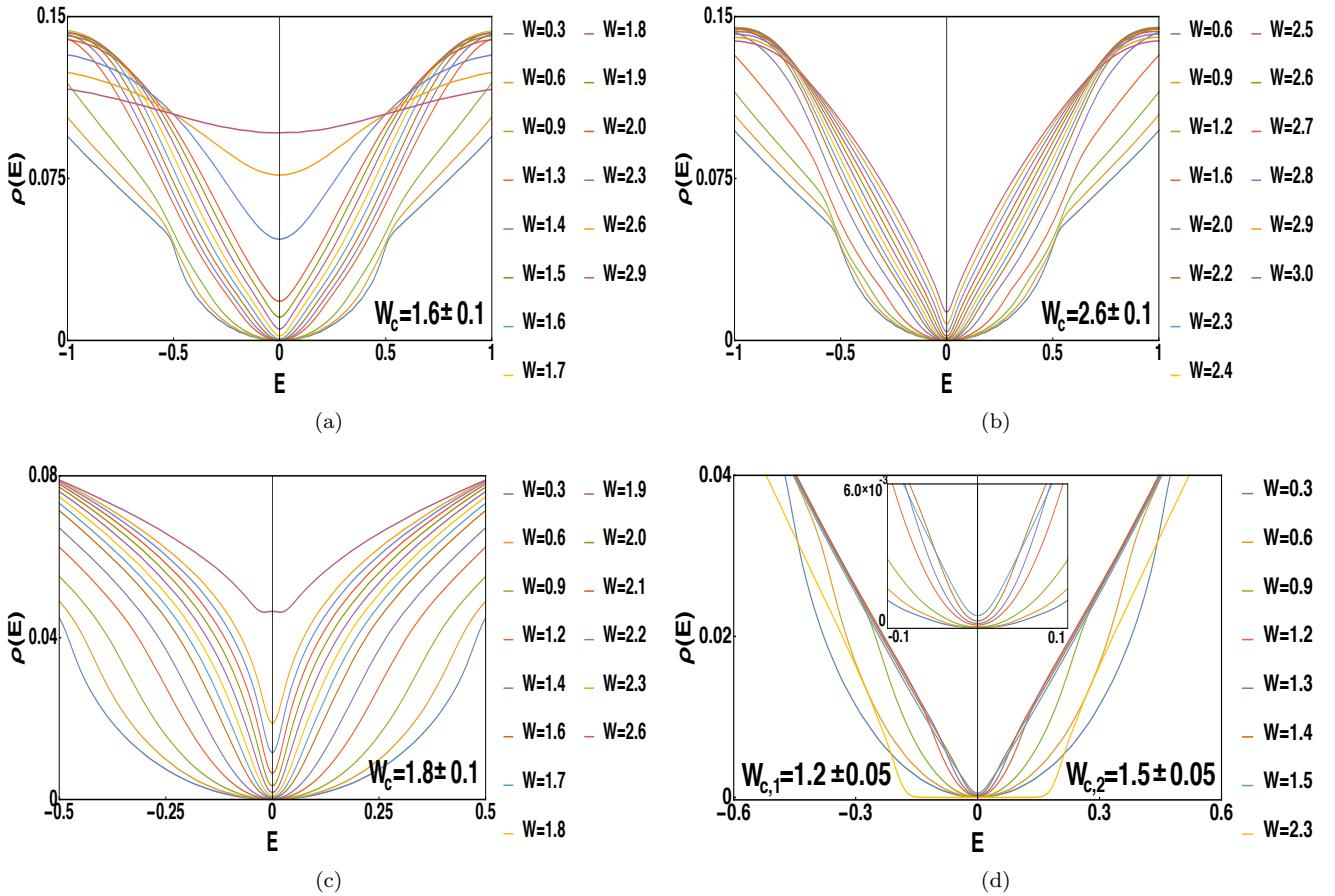


Figure 2: Scaling of numerically evaluated average density of states (ADOS) in dirty Weyl semimetals (WSMs) in the presence of (a) potential, (b) axial, (c) axial current and (d) current disorder for weak to strong disorder regime. Notice that for weak enough disorder  $\rho(E) \sim |E|^2$  for  $|E| \ll 1$ . In the metallic phase, setting for strong enough disorder, ADOS at zero energy  $\rho(0)$  becomes finite. Around a (non-universal) critical strength of disorder  $W = W_c$  the ADOS scales as  $\rho(E) \sim |E|$  for  $|E| \ll 1$ . Since  $\rho(E) \sim |E|^{\frac{d}{z}-1}$ , the dynamic scaling exponent  $z \approx 1.5$  across the WSM-metal quantum phase transitions (QPTs), irrespective of the nature of the elastic scatterers. All four disorders preserve the emergent global chiral symmetry, see Table II. Thus, scaling of ADOS strongly suggests the emergence of the *chiral superuniversality* across the WSM-metal QPTs, driven by chiral symmetric disorder. Numerically extracted critical exponents across WSM-metal QPTs and their comparison with the field theoretic predictions are displayed in Table I, suggesting an excellent agreement between these two methods. For current disorder, WSM-metal QPT at  $W = W_{c,1} = 1.20 \pm 0.05$  is immediately followed by a second QPT into the Anderson insulating phase for  $W > W_{c,2} = 1.50 \pm 0.05$ . Thus, even though the width of the metallic regime,  $W_{c,1} < W < W_{c,2}$ , is small [panel (d)], we still find  $\rho(E) \sim |E|$  and detect the onset of metallicity [inset of panel (d)]. The ADOS is numerically computed using the kernel polynomial method [68] in a cubic lattice of linear dimension  $L = 120$ . Lattice model is defined in Sec. II and for detailed analysis of ADOS see Sec. VI. In a suitably chosen lattice model the axial current disorder corresponds to magnetic impurities (Table II).

(i) in the field-theoretical framework by using two different renormalization-group (RG) schemes: (a) an  $\epsilon_m$ -expansion about a critical disorder distribution, where  $\epsilon_m = 1 - m$ , with the Gaussian white noise distribution realized as  $m \rightarrow 0$ , and (b)  $\epsilon_d = 2 - d$ -expansion about  $d_l = 2$ , the lower-critical spatial dimension for WSM-metal QPT, and (ii) lattice-based numerical evaluation of average DOS by using the *kernel polynomial method* (KPM) [68] in the presence of generic chiral symmetric disorder; see Fig. 2. Comparisons between the field theoretic predictions and numerical findings are given in

Table I. Our central results can be summarized as follows.

1. From the scaling analysis of disorder couplings, we show in Sec. IV that all types of disorder (both CSP and CSB) are irrelevant perturbations in a WSM. Such outcome is also substantiated numerically (Fig. 2), depicting that DOS scales as  $\rho(E) \sim |E|^2$  for small energy ( $E$ ), when disorder is weak.
2. We show in Sec. V that irrespectively of the details of two distinct  $\epsilon$ -expansions, in the presence of a CSP disorder, the WSM-metal QPT takes place

through either a QCP (when either potential or axial potential disorder is present) or a line of QCPs (when both types of scalar disorder are present), characterized by critical exponents

$$z = 1 + \frac{\epsilon}{2}, \quad \nu^{-1} = \epsilon, \quad (1)$$

obtained from the leading order in  $\epsilon$ -expansions, where  $\epsilon = \epsilon_m$  or  $\epsilon_d$ , and  $\epsilon = 1$  corresponds to the physical situation. Therefore, irrespective of the nature of elastic scatterers, the universality class of the WSM-metal QPT in the presence of a CSP disorder is unique, and we name such universality class *chiral superuniversality*.

3. In Sec. VI we carry out a thorough numerical analysis of DOS obtained by using KPM from a lattice model in the presence of all four CSP disorders (see Fig. 2). Within the numerical accuracy we find that  $z \approx 1.5$  and  $\nu \approx 1$  across possible CSP disorder driven WSM-metal QPTs (see Fig. 10 and also Table I). Thus numerically extracted values of critical exponents are in excellent agreement with the field theoretic predictions from leading order  $\epsilon$ -expansions, and strongly support the proposed scenario of emergent chiral superuniversality.
4. In Sec. VII we show that the CSB disorder can also drive a WSM-metal QPT through either an isolated QCP or a line of QCPs. Irrespective of the actual details of an  $\epsilon$ -expansion scheme, the values of the critical exponents at the QCP or line of QCPs in the presence of such disorder are in a stark contrast to the ones reported in Eq. (1), and typically  $z > d$ . The exact value of DSE depends on the regularization scheme. Most importantly, the DSE varies continuously across the line of QCPs supported by a strong CSB disorder, in contrast to the situation for CSP disorder. On the other hand,  $\nu^{-1} = \epsilon$  to the leading order in an  $\epsilon$  expansion, irrespective of the RG scheme.
5. In Sec. VIII, we show that various experimentally measurable quantities, such as average DOS, dynamic conductivity, specific heat and Grüneisen ratio, exhibit distinct scaling behavior in terms of CLE and DSE in different phases of a dirty WSM. As such, they may be useful to distinguish types of disorder in a WSM. Most importantly, distinct scaling of observables can allow to pin the onset of various phases in real materials.

It is worth mentioning that for sufficiently strong disorder the metallic phase in a Weyl system undergoes a second continuous QPT into an Anderson insulating phase [26, 51]. We, however, do not pursue such widely studied metal-insulator Anderson transition [69]. The rest of the paper is organized as follows. In Sec. II, we introduce a simple tight-binding model for a Weyl system

Disorder	Numerical Analysis			Field Theory	
	$W_c$	$z$	$\nu$	$z$	$\nu$
Potential	$1.6 \pm 0.1$	$1.45 \pm 0.05$	$0.99 \pm 0.05$	$3/2$	$1$
Axial	$2.6 \pm 0.1$	$1.47 \pm 0.06$	$1.06 \pm 0.06$	$3/2$	$1$
Magnetic	$1.8 \pm 0.1$	$1.51 \pm 0.06$	$1.05 \pm 0.06$	$3/2$	$1$
Current	$1.2 \pm 0.1$	$1.48 \pm 0.06$	$0.99 \pm 0.06$	$3/2$	$1$

Table I: Comparison of numerically extracted values of dynamic scaling exponent ( $z$ ) and correlation length exponent ( $\nu$ ) across the WSM-metal QPT, with the ones obtained from the leading order  $\epsilon$ -expansions using field theoretic techniques. All four disorders preserve continuous global chiral symmetry of a WSM. This comparison strongly suggests that a WSM-metal transition driven by a CSP disorder is insensitive to the nature of elastic scatterers, thus motivating an emergent chiral superuniversality class of the QPTs, as detailed in Sec. V.

and discuss possible phases and the phase transitions in the clean limit. In Sec. III, we demonstrate the effects of generic disorder near the clean WSM-insulator QCP, and perturbatively address the effects of strong disorder. In Sec. IV we set up the theoretical framework for addressing the role of randomness deep inside the WSM phase, and introduce the notion of  $\epsilon_m$  and  $\epsilon_d$  expansions for perturbative treatment of disorder. This section is rather technical and readers familiar with the formalism or interested in physical outcomes may wish to skip it. We devote Sec. V to the effects of CSP disorder and promote the notion of *chiral superuniversality*. Detailed numerical analysis on the scaling of DOS is presented in Sec. VI. Effects of CSB disorder are discussed in Sec. VII and scaling of various physical observables, such as DOS, specific heat, conductivity, etc., across the WSM-metal QPT is discussed in Sec. VIII. Concluding remarks and a summary of our main findings are presented in Sec. IX. Some additional technical details have been relegated to the Appendices.

## II. LATTICE MODEL FOR WEYL SYSTEM

Let us begin the discussion with a lattice realization of chiral Weyl fermions in a three-dimensional cubic lattice. Even though in most of the commonly known Weyl materials, such as the binary alloys TaAs and NbP, emergent Weyl fermions arise from complex band structures in noncentrosymmetric lattices, their salient features can be captured from a simple tight-binding model

$$H = \sum_{\mathbf{k}} \psi_{\mathbf{k}}^\dagger [\mathbf{N}(\mathbf{k}) \cdot \boldsymbol{\sigma}] \psi_{\mathbf{k}} \quad (2)$$

The two-component spinor is defined as  $\psi_{\mathbf{k}}^\top = (c_{\mathbf{k},\uparrow}, c_{\mathbf{k},\downarrow})$ , where  $c_{\mathbf{k},s}$  is the fermionic annihilation operator with momentum  $\mathbf{k}$  and spin/pseudospin projection  $s = \uparrow, \downarrow$ ,

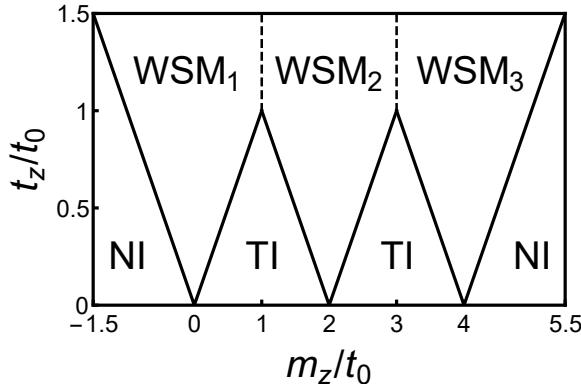


Figure 3: The phase diagram of the clean noninteracting tight-binding model defined through Eqs. (5) and (3). Here, NI and TI respectively represents trivial (normal) and Chern insulators. Weyl nodes in the WSM phase are always located along the  $k_z$  direction. Respectively WSM<sub>1,2,3</sub> supports one, two and one pair of Weyl nodes. The projection of the Weyl nodes on the  $xy$  plane in these phases are at the  $(0, 0)$  point,  $(0, \pi)$  and  $(\pi, 0)$  points, and  $(\pi, \pi)$  point. This model therefore supports *translationally active* topological phases. The transitions between the WSM and insulating phases (solid lines) and the ones between two distinct WSM phases (dashed lines) are continuous. We emphasize that there is no symmetry distinction among the phases.

and  $\sigma$  are standard Pauli matrices. We here choose

$$N_3(\mathbf{k}) = [t_z \cos(k_z a) - m_z] + t_0 [2 - \cos(k_x a) - \cos(k_y a)], \quad (3)$$

where  $a$  is the lattice spacing. The first term gives rise to two isolated Weyl nodes along the  $k_z$  axis at  $k_z = \pm k_z^0$ , where

$$\cos(k_z^0 a) = \frac{t_0}{t_z} \left[ \frac{m_z}{t_0} + \cos(k_x a) + \cos(k_y a) - 2 \right], \quad (4)$$

with the following choice of pseudospin vectors

$$N_1(\mathbf{k}) = t \sin(k_x a), \quad N_2(\mathbf{k}) = t \sin(k_y a). \quad (5)$$

The second term in Eq. (3), namely  $N_3^M(\mathbf{k}) = t_0 [2 - \cos(k_x a) - \cos(k_y a)]$ , plays the role of a momentum dependent *Wilson mass* [55, 56]. We subscribe to this tight-binding model in Sec. VI to numerically study the effects of randomness in a dirty WSM.

With the above chosen form of the Wilson mass only a single pair of Weyl nodes is realized at  $\mathbf{k}^0 = (0, 0, \pm k_z^0)$ , when  $\tilde{m}_z \leq 1$ , where  $\tilde{m}_z = m_z/t_0$ . For  $1 \leq \tilde{m}_z \leq 2$ , two pairs of Weyl nodes are found at  $(0, \pi, \pm k_z^0)$  and  $(\pi, 0, \pm k_z^0)$ . When  $\tilde{m}_z \geq 2$ , again a single pair of Weyl points is realized at  $(\pi, \pi, \pm k_z^0)$ . Notice that when  $\tilde{t}_z < 1$  three distinct realizations of WSM phase are separated by intervening insulating phases, representing three dimensional Chern insulator, while the insulating phases realized for  $\tilde{m}_z < -1$  and  $\tilde{m}_z > 4$  are topologically trivial. Hence, by tuning  $\tilde{m}_z$  one can drive the system

through WSM-insulator QPT as long as  $\tilde{t}_z < 1$ , where  $\tilde{t}_z = t_z/t_0$ . However, for  $\tilde{t}_z > 1$  the noninteracting model supports only trivial insulating phases when  $\tilde{m}_z/\tilde{t}_z < -1$  or  $(\tilde{m}_z - 4)/\tilde{t}_z > 1$ . Direct and continuous transitions between two different WSMs take place without an intervening insulating phase when  $\tilde{t}_z > 1$ . Therefore, our proposed model in Eqs. (5) and (3) supports translationally active topological phases with band-inversions at non- $\Gamma$  points in the Brillouin zone [9, 70] and the resulting phase diagram is shown in Fig. 3.

For the sake of simplicity, we hereafter only consider the parameter regime  $-1 < \tilde{m}_z < 1$  and  $\tilde{t}_z < 1$ , so that only a single pair of Weyl fermions is realized at  $\mathbf{k}^0 = (0, 0, \pm \cos^{-1} |m_z/t_z|)$ . In the vicinity of these two points the Weyl quasiparticles can be identified as left and right chiral fermions. A Weyl semimetal can be found when  $|m_z/t| \leq 1$  and the system becomes an insulator for  $|m_z/t| > 1$ . Even though we here restrict our analysis within the aforementioned parameter regime, this analysis can be generalized to study the semimetal-insulator QPTs in various other regimes shown in Fig. 3.

Within this parameter regime, to capture the Weyl semimetal-insulator QPT which occurs along the line  $\tilde{t}_z/\tilde{m}_z = 1$ , we expand the tight-binding model around the  $\Gamma = (0, 0, 0)$  point of the Brillouin zone to arrive at the effective low energy Hamiltonian

$$\hat{H}_Q(\Delta) = v (\sigma_1 k_x + \sigma_2 k_y) + \sigma_3 (b k_z^2 - \Delta), \quad (6)$$

where  $v = ta$  is the Fermi velocity in the  $xy$  plane and  $b = t_z a^2/2$  bears the dimension of inverse mass. For  $\Delta = t_z - m_z < 0$  the system becomes an insulator (Chern or trivial). On the other hand, when  $\Delta > 0$ , the lattice model describes a WSM. The QPT in this clean model between these two phases takes place at  $\Delta = 0$ . Hence,  $\Delta$  plays the role of a tuning parameter across the WSM-insulator QPT. The QCP separating these two phases is described by an *anisotropic* semimetal, captured by the Hamiltonian  $H_Q(0)$  in Eq. (6), that in turn also determines the universality class of the transition. Notice that the expansion of the lattice Hamiltonian (5) also yields terms  $\sim k_x^2$  and  $\sim k_y^2$  and higher order (from the Wilson mass), which are, however, irrelevant in the RG sense, and therefore do not affect the critical theory for the WSM-insulator QPT. Hence, we omit these higher gradient terms. Next we address the stability of this quantum critical semimetal against the disorder in the system using scaling theory and RG analysis.

### III. EFFECTS OF DISORDER ON SEMIMETAL-INSULATOR TRANSITION

The imaginary time ( $\tau$ ) action associated with the low

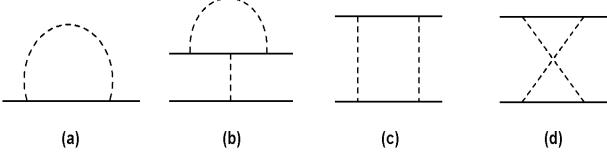


Figure 4: One-loop diagrams contributing to the self-energy correction [(a)], and renormalization of disorder coupling [(b)-(d)]. Notice that contributions from (c) ladder and (d) crossing diagram are ultraviolet divergent only in  $\epsilon_n$  (Sec. III A) and  $\epsilon_d$  (Sec. IV C) expansions, while they produce ultraviolet finite contribution in  $\epsilon_m$  expansion (Sec. IV B). Here, solid (dashed) lines represent fermionic (disorder) field.

energy Hamiltonian (6) reads as

$$S_0 = \int d\tau d^2x_\perp dx_3 \psi^\dagger [\partial_\tau - iv\partial_j \sigma_j - \sigma_3 (b\partial_3^2 + \Delta)] \psi. \quad (7)$$

In the proximity to the Weyl semimetal-insulator QPT, the system can be susceptible to random charge impurities and random magnetic impurities, and their effect can be captured by the action

$$S_D = \int d\tau d^2x_\perp dx_3 \psi^\dagger [V_0(\mathbf{x})\sigma_0 + V_\perp(\mathbf{x})(\sigma_1 + \sigma_2) + V_z(\mathbf{x})\sigma_3] \psi, \quad (8)$$

where  $V_j(\mathbf{x})$  are random variables. The effect of random charge impurities is captured by  $V_0(\mathbf{x})$ , while  $V_\perp(\mathbf{x})$  and  $V_z(\mathbf{x})$  represents random magnetic impurities with the

magnetic moment residing in the easy or  $xy$  plane and in the  $z$  direction (denoted here by  $x_3$  for notational clarity), respectively, which we allow due to the anisotropy of the Hamiltonian (6). All types of disorder are assumed to be characterized by Gaussian white noise distributions.

The scale invariance of the noninteracting action (7) mandates the following scaling ansatz:  $\tau \rightarrow e^l \tau$ ,  $(x, y) \rightarrow e^l (x, y)$  and  $x_3 \rightarrow e^{l/2} x_3$ , followed by the rescaling of the field operator  $\psi \rightarrow e^{-5l/4} \psi$ , where  $l$  is the running RG scale. The scaling dimension of the tuning parameter  $\Delta$  is then given by  $[\Delta] = 1$ , implying that  $\Delta$  is a relevant perturbation at the WSM-insulator QCP, located at  $\Delta = 0$ . The scaling dimension of the tuning parameter  $\Delta$  plays the role of the *correlation length exponent* ( $\nu$ ) at this QCP, implying  $\nu = 1$ . In the presence of disorder, as we show in Appendix A, the Harris stability criterion [25] can be generalized to the WSM-insulator QCP with the quantum-critical theory of the form given by Eq. (6), but with the topological charge  $c$ , which turns out to be stable against weak disorder if  $\nu > 2/d_*$ , with  $2/d_* = 4c/(4+c)$ , and  $d_*$  as the *effective spatial dimensionality* of the system. At the WSM-insulator QCP  $\nu = 1$ , and the critical excitations residing at  $\Delta = 0$  are therefore stable against weak disorder when  $c = 1$  (regular WSM). We next analyze the effects of disorder on the WSM-insulator QCP using a RG approach.

### A. Perturbative RG analysis

After performing the disorder averaging in the action (8) within the replica formalism, we arrive at the Euclidean action

$$\bar{S} = \int d\tau d^2x_\perp dx_3 \psi_a^\dagger [\partial_\tau - iv(\partial_x \sigma_1 + \partial_y \sigma_2) + \sigma_3 [(-i)^n b_n \partial_3^n - \Delta]] \psi_a - \int d\tau d\tau' d^2x_\perp dx_3 \left[ \frac{\Delta_0}{2} (\psi_a^\dagger \psi_a)_{(\mathbf{x}, \tau)} (\psi_b^\dagger \psi_b)_{(\mathbf{x}, \tau')} \right. \\ \left. + \frac{\Delta_\perp}{2} \sum_{j=1,2} (\psi_a^\dagger \sigma_j \psi_a)_{(\mathbf{x}, \tau)} (\psi_b^\dagger \sigma_j \psi_b)_{(\mathbf{x}, \tau')} + \frac{\Delta_z}{2} (\psi_a^\dagger \sigma_3 \psi_a)_{(\mathbf{x}, \tau)} (\psi_b^\dagger \sigma_3 \psi_b)_{(\mathbf{x}, \tau')} \right], \quad (9)$$

where  $a, b$  are replica indices. Notice that here we have replaced  $k_3^2 \rightarrow k_3^n$ , with  $n$  as an integer. We we will show that such deformation of the quasiparticle spectrum allows us to control the perturbative calculation in terms of disorder coupling. The above imaginary-time action ( $\bar{S}$ ) remains invariant under the space-time scaling  $(x, y) \rightarrow e^l (x, y)$ ,  $x_3 \rightarrow e^{l/n} x_3$  and  $\tau \rightarrow e^{z_l} \tau$ . At the bare level the scale invariance of the free part of the action requires the field renormalization factor  $Z_\psi = e^{-(2+1/n)l}$  and  $\psi \rightarrow Z_\psi^{-1/2} \psi$ . From this scaling analysis we immediately find that the scaling dimension of disorder couplings is  $[\Delta_j] = -1/n$ , for  $j = 0, \perp, z$ . Therefore, at the WSM-insulator QCP, characterized by  $n = 2$ , disorder is an ir-

relevant perturbation, in accordance with the prediction from the *generalized Harris criterion*, implying the stability of this QCP against sufficiently weak randomness. Note that disorder couplings are a *marginal* in a *hypothetical* limit  $n \rightarrow \infty$ , for which the system effectively becomes a *two-dimensional Weyl semimetal*. Therefore, perturbative analysis in the presence of generic disorder is controlled via an  $\epsilon_n$ -expansion, where  $\epsilon_n = 1/n$ , about  $n \rightarrow \infty$ , following the spirit of an  $\epsilon$ -expansion [71, 72].

Upon integrating out the fast fourier modes within the momentum shell  $\Lambda e^{-l} < k_\perp < \Lambda$ , where  $k_\perp = \sqrt{k_x^2 + k_y^2}$ ,  $0 < k_3^2 < \infty$  and accounting for pertubative corrections to one-loop order (Fig. 4), we arrive at the following flow

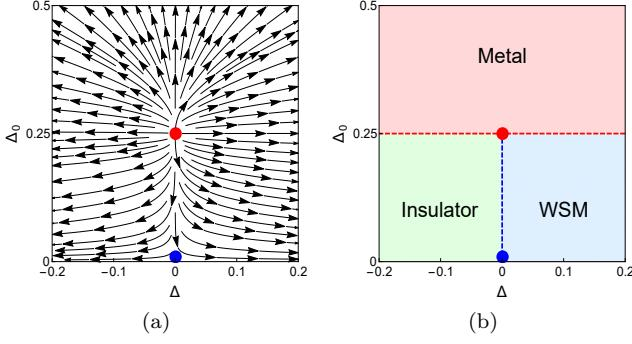


Figure 5: (a) The RG flow diagram obtained from Eq. (10) and (b) the resulting phase diagram in the  $\Delta - \Delta_0$  plane, for  $\epsilon_n = 1/2$ . Here,  $\Delta$  is the tuning parameter for WSM-insulator transition [see Eq. (6)], and  $\Delta_0$  is the strength of random charge impurities. Blue and red dot respectively represents a critical and a multicritical point. The metallicity sets in through the multicritical point.

equations

$$\begin{aligned} \beta_X &= X [z - 1 - (\Delta_0 + 2\Delta_\perp + \Delta_z)], \\ \beta_\Delta &= \Delta [1 + \Delta_0 - 2\Delta_\perp + \Delta_z], \\ \beta_{\Delta_0} &= -\epsilon_n \Delta_0 + 2\Delta_0 (\Delta_0 + 2\Delta_\perp + \Delta_z) \\ \beta_{\Delta_\perp} &= -\epsilon_n \Delta_\perp + 2\Delta_0 \Delta_3 \\ \beta_{\Delta_z} &= -\epsilon_n \Delta_z + 2\Delta_3 (2\Delta_\perp - \Delta_0 - \Delta_z) + 4\Delta_0 \Delta_\perp, \end{aligned} \quad (10)$$

in terms of dimensionless parameters

$$\hat{\Delta} = \frac{\Delta}{v\Lambda}, \quad \hat{\Delta}_j = \Delta_j \left[ \frac{\Lambda^{\epsilon_n}}{(2\pi)^2 b_n^{\epsilon_n} v^{2-\epsilon_n}} \right],$$

for  $X = v, b_n, j = 0, \perp, z$ ,  $\beta_Q \equiv dQ/dl$  is the  $\beta$ -function for the running parameter  $Q$ , and for brevity we omit the *hat* notation in Eq. (10). In the above flow equation, we have kept only the leading divergent contribution that survives as  $n \rightarrow \infty$ . Inclusion of subleading divergences only leads to nonuniversal corrections, as shown in Appendix B. The marginality condition for in-plane Fermi velocity ( $v$ ) and  $b_n$  leads to a scale dependent DSE

$$z(l) = 1 + (\Delta_0 + 2\Delta_\perp + \Delta_3)(l). \quad (11)$$

The coupled RG flow equations (10) support only two fixed points:

- $(\Delta, \Delta_0, \Delta_\perp, \Delta_3) = (0, 0, 0, 0)$ , which has only one unstable direction along the  $\Delta$ -direction that serves as the tuning parameter for WSM-insulator QPT. This fixed point stands as a QCP in the four dimensional coupling constant space. The correlation length exponent at this QCP is  $\nu^{-1} = 1$ . All disorder couplings are irrelevant perturbations at this QCP.
- $(\Delta, \Delta_0, \Delta_\perp, \Delta_3) \approx (0, \epsilon_n/2, 0, 0)$  stands as a multicritical point with two unstable directions. At this

multicritical point the WSM, an insulator and the metallic phase meet. Two correlation-length exponents are  $\nu_M^{-1} = \epsilon_n$  determining the relevance of disorder coupling  $\Delta_0$ , which drives the anisotropic critical semimetal into a diffusive metallic phase, and  $\nu^{-1} = 1$  that determines the relevance of the tuning parameter  $\Delta$ , controlling the WSM-insulator transition. The DSE for critical semimetal-metal QPT is  $z = 1 + \frac{\epsilon_n}{2}$ . Therefore, for a three-dimensional anisotropic critical semimetal-metal, setting  $\epsilon_n = 1/2$ , the critical exponents are  $\nu_M = 2$  and  $z = 1.25$ .

The RG flow and the resulting phase diagrams are shown in Fig. 5(a) and 5(b), respectively. At the multicritical point the average DOS scales as  $\varrho(E) \sim |E|^{d/z-1} \approx |E|^{1.4}$  to one-loop order. Beyond the critical strength of disorder system becomes a metal where the average DOS at zero energy [ $\varrho(0)$ ] is finite and the order parameter exponent  $\beta = (d-z)\nu = 3.5$  determines the scaling of  $\varrho(0)$  according to  $\varrho(0) \sim \delta^\beta = \delta^{3.5}$ , where  $\delta = (\Delta_0 - \Delta_0^*)/\Delta_0^*$  is the reduced disorder coupling from the critical one at  $\Delta_0 = \Delta_0^*$ . Thus we expect such multicritical point to be generically stable. Next we address the effects of disorder inside the WSM phase, with renormalized  $\Delta > 0$ .

#### IV. DIRTY WEYL SEMIMETAL: MODEL AND SCALING ANALYSIS

In this section, we set up the theoretical framework to analyze the role of disorder when the system is deep inside the WSM phase. We will introduce the notion of two different  $\epsilon$  expansions: (a) an  $\epsilon_m$ -expansion about a critical disorder distribution, where  $\epsilon_m = 1 - m$  with Gaussian white noise distribution recovered as  $m \rightarrow 0$ ; (b) an  $\epsilon_d$ -expansion about the lower critical dimension  $d_c = 2$  for WSM-metal QPT, where  $\epsilon_d = d - 2$ , and therefore for three spatial dimensions  $\epsilon_d = 1$ .

##### A. Hamiltonian and action

The effective low energy description of WSM can be obtained by expanding the lattice Hamiltonian (5) around the Weyl nodes located at  $\mathbf{k}^0 = (0, 0, \pm k_z^0)$ , with  $k_z^0 = \cos^{-1}(\frac{m_z}{t_z})$ . The resulting low energy Hamiltonian reads

$$H_W = \tau_0 \otimes v (k_x \sigma_1 + k_y \sigma_2) + \tau_3 \otimes \sigma_3 v_z k_z, \quad (12)$$

where  $v = ta$ ,  $v_z = a\sqrt{t_z^2 - m_z^2}$ , and the momentum is measured from the Weyl nodes. For simplicity we hereafter take the Fermi velocity to be isotropic,  $v = v_z$ , so that the low energy Hamiltonian becomes rotationally symmetric. Upon performing a unitary rotation with  $U = \sigma_0 \oplus \sigma_3$ , the above Hamiltonian assumes a quasirelativistic form  $H_W = i\gamma_0 \gamma_j v k_j$ , where  $\gamma_0 = \tau_1 \otimes \sigma_0$ ,

$\gamma_j = \tau_2 \otimes \sigma_j$  for  $j = 1, 2, 3$  are mutually anti-commuting  $4 \times 4$  Hermitian matrices, and summation over repeated spatial indices is assumed. To close the Clifford algebra of five mutually anticommuting matrices we define  $\gamma_5 = \tau_3 \otimes \sigma_0$ . Two sets of Pauli matrices  $\sigma_\mu$  and  $\tau_\mu$  respectively operate on spin and valley or chiral (left and right) indices. The low energy effective Hamiltonian enjoys variety of *emergent* discrete and continuous symmetries. The above Hamiltonian is invariant under a pseudo-time-reversal symmetry, generated by anti-unitary operator  $\mathcal{T} = \gamma_0 \gamma_2 K$ , where  $K$  is the complex conjugation, a charge conjugation symmetry, generated by  $\mathcal{C} = \gamma_2$ , and parity or inversion symmetry generated by  $\mathcal{P} = \gamma_0$ . Furthermore, the Hamiltonian (12) also possesses a global chiral  $U(1)$  symmetry, generated by  $\gamma_5$ , which in the low energy limit corresponds to the generator of translational symmetry [62].

To incorporate the effects of disorder we consider the following minimal continuum action for a dirty WSM

$$S = \int d^d \mathbf{x} d\tau [\bar{\Psi}(\gamma_0 \partial_\tau + v \gamma_j \partial_j) \Psi - \varphi_N(\bar{\Psi} N \Psi)], \quad (13)$$

with  $\mathbf{x}$  as  $d$ -dimensional spatial coordinates, the four-component spinor  $\Psi^\dagger = (u_{\uparrow,+}^\dagger, u_{\downarrow,+}^\dagger, u_{\uparrow,-}^\dagger, u_{\downarrow,-}^\dagger)$ , where  $u_{\sigma,\tau}^\dagger$  is the fermionic creation operator near the Weyl point at  $\tau \mathbf{k}^0$  for  $\tau = \pm$  (left/right) and with spin  $\sigma = \uparrow, \downarrow$ , while  $\bar{\Psi} = \Psi^\dagger \gamma_0$ , as usual. The disorder field  $\varphi_N$  is coupled to the fermion bilinears realized with different choices of  $4 \times 4$  matrices,  $N$ , as shown in Table II. Notice that the matrices associated with four types of disorder anticommute with  $\gamma_5$  and represent chiral symmetric disorder, while for the other four types of disorder  $[N, \gamma_5] = 0$  and the corresponding disorder vertex breaks the  $U(1)$  chiral symmetry. *As we demonstrate in this paper, this global chiral symmetry plays a fundamental role in classifying the disorder-driven WSM-metal QPTs.*

### B. $\epsilon_m$ expansion in three dimensions

We assume that the disorder field obeys the distribution [36, 73]

$$\langle \varphi_N(\mathbf{x}) \varphi_N(\mathbf{y}) \rangle = \Delta_N \frac{1}{|\mathbf{x} - \mathbf{y}|^{d-m}}, \quad (14)$$

or in the momentum space

$$\langle \varphi_N(\mathbf{q}) \varphi_N(\mathbf{0}) \rangle = \tilde{\Delta}_N \frac{1}{|\mathbf{q}|^m}, \quad (15)$$

and the limit  $m \rightarrow 0$  corresponds to the Gaussian white noise distribution, which we are ultimately interested in. This form of the white noise distribution stems from the following representation of the  $d$ -dimensional  $\delta$ -function [41]

$$\delta^{(d)}(\mathbf{x} - \mathbf{y}) = \lim_{m \rightarrow 0} \frac{\Gamma(\frac{d-m}{2})}{2^m \pi^{d/2} \Gamma(m/2)} \frac{1}{|\mathbf{x} - \mathbf{y}|^{d-m}}. \quad (16)$$

Bilinear	Physical quantity	$\mathcal{T}$	$\mathcal{P}$	$U_c$	$\mathcal{C}$	Coupling
$\bar{\Psi} \gamma_0 \Psi$	chemical potential	✓	✓	✓	✗	$\Delta_V$
$\bar{\Psi} \gamma_0 \gamma_5 \Psi$	axial potential	✓	✗	✓	✓	$\Delta_A$
$\bar{\Psi} \Psi$	scalar mass	✗	✓	✗	✓	$\Delta_S$
$\bar{\Psi} i \gamma_5 \Psi$	pseudo-scalar mass	✓	✗	✗	✓	$\Delta_{PS}$
$\bar{\Psi} i \gamma_5 \gamma_j \Psi$	axial current	✗	✓	✓	✓	$\Delta_M$
$\bar{\Psi} i \gamma_j \Psi$	current	✗	✗	✓	✗	$\Delta_C$
$\bar{\Psi} i \Sigma_{0j} \Psi$	temporal tensor	✗	✗	✗	✗	$\Delta_{SO}$
$\bar{\Psi} \Sigma_{jk} \Psi$	spatial tensor	✓	✓	✗	✗	$\Delta_{AM}$

Table II: Various types of disorder represented by fermionic bilinears ( $j = 1, 2, 3$ ), together with their symmetries under pseudo time-reversal ( $\mathcal{T}$ ), parity ( $\mathcal{P}$ ), continuous chiral rotation ( $U_c$ ) and charge-conjugation ( $\mathcal{C}$ ). The disorder couplings are represented by  $\Delta_N$  and  $\Sigma_{\mu\nu} = [\gamma_\mu, \gamma_\nu]/(2i)$ . Note that true time-reversal symmetry in WSM is already broken. The pseudo time-reversal symmetry  $\mathcal{T}$  is generated by an anti-unitary operator  $\gamma_0 \gamma_2 K$ , where  $K$  is complex conjugation, such that  $\mathcal{T}^2 = -1$  (The true time-reversal operator is  $\gamma_1 \gamma_3 K$ ). The parity operator is  $\mathcal{P} = \gamma_0$ , while the charge-conjugation operator is  $\mathcal{C} = \gamma_2$ . The continuous chiral symmetry ( $U_c$ ) is generated by  $\gamma_5$ , the generator of translational symmetry in the continuum limit in a clean Weyl semimetal [62]. Here ✓ and ✗ signify even and odd under a symmetry operation, respectively. With a slightly different tight-binding model, where  $N_j(\mathbf{k}) = t \cos(k_j a)$  and  $N_3^M(\mathbf{k}) = (\sin(k_1 a) + \sin(k_2 a) - 2 \sin(k_3 a))$ , the axial current corresponds to magnetization, temporal and spatial tensors to spin-orbit and axial magnetization, respectively. However, such microscopic details do not alter any physical outcome.

We now carry out the scaling analysis of the continuum action for a WSM given by Eq. (13). The scaling dimensions of the momentum and frequency are  $[q] = 1$ , and  $[\omega] = z$ . The form of the Euclidean action (13) then implies that the engineering scaling dimension of the fermionic field  $[\Psi] = d/2$  and  $[v] = z - 1$ , while the scaling dimension of the disorder field is  $[\varphi_N] = z + \eta_{\varphi_N}$ , since the engineering dimension of the disorder field is equal to the DSE  $z$  for any choice of  $N$ , and  $\eta_{\varphi_N}$  is its anomalous dimension. Eq. (14) then yields

$$[\Delta_N] = 2(z + \eta_{\varphi_N}) - d + m. \quad (17)$$

Due to linearly dispersing low-energy quasiparticles, a WSM corresponds to  $z = 1$  fixed point, and in  $d = 3$  the engineering dimension of the disorder strength is  $[\Delta_N] = m - 1$ . A first implication of this result is that the white noise disorder,  $m = 0$ , is *irrelevant* close to the WSM ground state in  $d = 3$ . Second, for  $m = 1$ , the disorder is marginal and we use that to introduce the deviation from this value as an expansion parameter  $\epsilon_m = 1 - m$ .

The  $\beta$ -function (infrared) for the disorder coupling  $\Delta_N$  in the  $\epsilon_m$  expansion is given in terms of its scaling dimension in Eq. (17), yielding

$$\beta_{\Delta_N} = \Delta_N [-\epsilon_m + 2(z - 1) + 2\eta_{\varphi_N}], \quad (18)$$

in  $d = 3$ . Therefore, to obtain the explicit form of this  $\beta$ -function in terms of the disorder couplings, we have to compute the DSE and the anomalous dimension of the

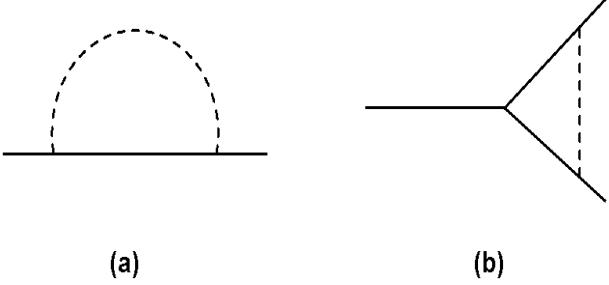


Figure 6: One-loop (a) self-energy and (b) vertex diagram. Contributions from only these two diagrams are ultraviolet divergent in  $\epsilon_m = m - 1$  expansion. Evaluations of these two diagrams are shown in Appendix C. Here, solid (dashed) lines represent fermion (disorder) fields.

disorder field. The former is obtained from the fermion self-energy with the diagram shown in Fig. 6(a), while the latter is found from the vertex diagram in Fig. 6(b). Evaluation of these two diagrams have been carried out using field-theoretic method (see Appendix C). Alternatively, one may choose to integrate out the fast modes within the momentum shell  $\Lambda e^{-l} < k < \Lambda$ , with  $\Lambda$  as an ultraviolet cutoff in the momentum, to arrive at the RG flow equations for  $\Delta_N$ .

### 1. Self-energy and dynamic scaling exponent

We first show the computation of the self-energy diagram, shown in Fig. 6(a), yielding the dynamical exponent and the anomalous dimension for the fermion field within the regularization scheme defined by the parameter  $\epsilon_m = 1 - m$ , the deviation from the critical disorder distribution. All the integrals are therefore performed in  $d = 3$ . The divergent part of the integral appears as a pole  $\sim 1/\epsilon_m$ , analogously to the case of the dimensional regularization where the deviation from the upper or lower critical space-time dimension plays the role of an expansion parameter, as in the  $\epsilon_d$  regularization scheme. To find renormalization constants, we use minimal subtraction, i.e. we keep only divergent part appearing in the corresponding diagrams.

The action (13) without the disorder yields the inverse free fermion propagator  $G_0^{-1}(i\omega, \mathbf{k}) = i(\gamma_0\omega + v\gamma_j k_j)$ . Taking into account the self-energy correction, the inverse dressed fermion propagator is

$$G^{-1}(i\omega, \mathbf{k}) = G_0^{-1}(i\omega, \mathbf{k}) + \Sigma(i\omega, \mathbf{k}), \quad (19)$$

with  $\Sigma(i\omega, \mathbf{k})$  as the self-energy. After accounting for all possible disorders, we arrive at the following compact expression for the self-energy (see Appendix C for details)

$$\Sigma(i\omega, \mathbf{k}) = i\gamma_0\omega \left( \frac{f_1(\Delta_j)}{\epsilon_m} \right) + iv\gamma_j k_j \left( \frac{f_2(\Delta_j)}{3\epsilon_m} \right), \quad (20)$$

where

$$f_1(\Delta_j) = \Delta_V + \Delta_A + 3\Delta_M + 3\Delta_C + 3\Delta_{SO} + 3\Delta_{AM} + \Delta_S + \Delta_{PS}, \quad (21)$$

$$f_2(\Delta_j) = -\Delta_V - \Delta_A + \Delta_M + \Delta_C - \Delta_{SO} - \Delta_{AM} + \Delta_S + \Delta_{PS}, \quad (22)$$

with  $\hat{\Delta}_j = \Delta_j k^{\epsilon_m} / (2\pi^2 v^2)$ , and for brevity we here drop the hat symbol in the final expression. From the above expression of the self-energy, together with the renormalization condition  $G^{-1}(\omega, \mathbf{k}) = Z_\Psi(i\gamma_0\omega + Z_v v_0 i\gamma_j k_j)$ , with  $v_0$  as the bare Fermi velocity, we arrive at the expression for the fermion-field renormalization ( $Z_\Psi$ ) and velocity renormalization ( $Z_v$ )

$$Z_\Psi = 1 + \frac{f_1(\Delta_j)}{\epsilon_m}, \quad Z_v = 1 - \frac{1}{\epsilon_m} \left[ f_1(\Delta_j) - \frac{f_2(\Delta_j)}{3} \right]. \quad (23)$$

This equation then yields the anomalous dimension for the fermion field

$$\eta_\Psi = - \sum_j \frac{d \ln Z_\Psi}{d \Delta_j} \beta_{\Delta_j}. \quad (24)$$

Furthermore, the renormalization factor  $Z_v$  enters the renormalization condition for the Fermi velocity  $Z_v v_0 = v$ , with  $v$  as the renormalized Fermi velocity. Using Eq. (23), together with  $\beta_{\Delta_N} = -\epsilon_m \Delta_N + \mathcal{O}(\Delta_j^2)$ , yields

$$\beta_v = \frac{1}{3}v [3f_1(\Delta_j) - f_2(\Delta_j)]. \quad (25)$$

Finally, since  $[v] = z - 1$ , the  $\beta$ -function of the Fermi velocity is  $\beta_v = (z - 1)v$ , which together with Eq. (25) determines the DSE

$$z = 1 + \frac{1}{3} [3f_1(\Delta_j) - f_2(\Delta_j)]. \quad (26)$$

### 2. Vertex correction: Anomalous dimension of disorder field

We now turn to the vertex correction due to the disorder, shown in Fig. 6(b), which yields the anomalous dimension of the disorder field. As shown in Appendix C, the vertex represented by the matrix  $N$  receives the correction of the form

$$V_N(\mathbf{k}) = \sum_M [M \gamma_j N \gamma_j M] \frac{\Delta_M}{3\epsilon_m}. \quad (27)$$

The corresponding renormalization condition that determines the renormalization constant  $Z_{\varphi_N}$  for the disorder field reads

$$Z_\Psi Z_{\varphi_N} N + V_N = N, \quad (28)$$

with  $Z_\Psi$  given by Eq. (23). The above condition in turn yields the anomalous dimension of the disorder field as

$$\eta_{\varphi_N} = - \sum_j \frac{d \ln Z_{\varphi_N}}{d \Delta_j} \beta_{\Delta_j}, \quad (29)$$

which we then use to write the explicit form of the  $\beta$ -function Eq. (18) in terms of the disorder couplings.

### C. $\epsilon_d$ -expansion about $d = 2$

Alternatively, one may take the Gaussian white noise distribution in Eq. (14) with  $m \rightarrow 0$  from the outset. In that case, the engineering dimension of the disorder coupling is equal to  $2 - d$ , since  $z = 1$  in a clean WSM. Therefore,  $d = 2$  is the *lower* critical dimension in the problem and we can use  $\epsilon_d = d - 2$  as an expansion parameter, following the spirit of  $\epsilon$ -expansion [28, 34, 35, 38, 39, 42, 53, 71]. In this scheme, after performing the disorder averaging using the replica method, the imaginary time action assumes a similar form of Eq (9).

Within the framework of the  $\epsilon_d$  expansion only the temporal (frequency-dependent) component of self energy acquires a disorder-dependent correction to the leading order. The self-energy correction due to disorder reads as

$$\Sigma(i\omega, \mathbf{k}) = i\gamma_0\omega \left( \frac{f_1(\Delta_j)}{\epsilon_d} \right), \quad (30)$$

with the function  $f_1(\Delta_j)$  given by Eq. (21), and  $\Delta_j \Lambda^{\epsilon_d} / (2\pi v^2) \rightarrow \Delta_j$ . This result is obtained from Eq. (C1) with  $d = 2 + \epsilon_d$  and  $m = 0$ . As a result, the field renormalization factor  $Z_\Psi = 1 + f_1(\Delta_j)/\epsilon_d$  and the velocity renormalization factor is  $Z_v = 1 - f_1(\Delta_j)/\epsilon_d$ . Using the renormalization condition  $Z_v v_0 = v$ , together with  $\beta_{\Delta_N} = -\epsilon_d \Delta_N + \mathcal{O}(\Delta_j^2)$ , we obtain the leading order RG flow equation for the Fermi velocity

$$\beta_v = v(z - 1) = v f_1(\Delta_j), \quad (31)$$

which yields a scale dependent dynamic exponent  $z = 1 + f_1(\Delta_j)$ . The seemingly different expressions for the flow equation and DSE in these two schemes stems from underlying different methodology of capturing the ultra-violet divergences of various diagrams.

## V. CHIRAL SYMMETRIC DISORDER

We first focus on chiral-symmetric disorders. For a single pair of Weyl fermions there are four such disorders, namely chemical potential, axial potential, current and axial current disorders, as shown in Table II. With

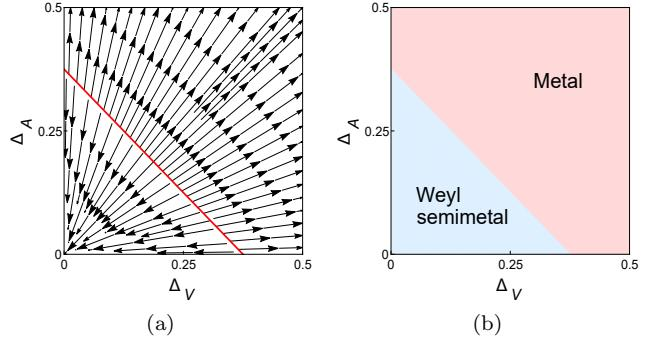


Figure 7: (a) The RG flow diagram and (b) the phase diagram in the  $\Delta_V - \Delta_A$  plane, for  $\epsilon_m = 1$ , obtained from Eq. (32). Here  $\Delta_V$  and  $\Delta_A$  are respectively the strength of potential and axial potential disorder. The red line in (a) corresponds to the line of quantum critical points [see Eq. (33)] that in turn defines the phase boundary between the Weyl semimetal and metallic phases, as shown in panel (b). A similar flow and phase diagram is obtained from the RG calculation performed within the framework of an  $\epsilon_d$  expansion [see Eq. (36)] [28, 39, 41].

appropriate lattice model axial current disorder corresponds to magnetic impurities and from here onward we use this terminology. We will address the effect of weak and strong chiral symmetric disorder using both  $\epsilon_m$  and  $\epsilon_d$  expansions.

### A. $\epsilon_m$ expansion

Let us first analyze this problem pursuing the  $\epsilon_m$  expansion. Using Eqs. (18), (26), (28) and (29), we obtain the following RG flow equations for the coupling constants to the leading order in  $\epsilon_m$

$$\begin{aligned} \beta_{\Delta_V} &= \Delta_V \left[ -\epsilon_m + \frac{8}{3} (\Delta_V + \Delta_A) + \frac{16}{3} (\Delta_C + \Delta_M) \right], \\ \beta_{\Delta_A} &= \Delta_A \left[ -\epsilon_m + \frac{8}{3} (\Delta_V + \Delta_A) + \frac{16}{3} (\Delta_C + \Delta_M) \right], \\ \beta_{\Delta_M} &= -\epsilon_m \Delta_M, \quad \beta_{\Delta_C} = -\epsilon_m \Delta_C. \end{aligned} \quad (32)$$

The above set of flow equations supports a *line of quantum critical points* in the  $\Delta_V - \Delta_A$  plane, determined by

$$\Delta_{V,*} + \Delta_{A,*} = \frac{3}{8} \epsilon_m, \quad (33)$$

where the quantities with subscript “\*” represent their critical values for WSM-metal QPT. The RG flow in this plane is shown in Fig. 7(a). The line of QCPs also determines the WSM-metal phase boundary, and the corresponding phase diagram in the  $\Delta_V - \Delta_A$  plane is shown in Fig. 7(b). At each point of this line of QCPs the DSE and CLE are respectively given by

$$z = 1 + \frac{\epsilon_m}{2}, \quad \nu^{-1} = \epsilon_m. \quad (34)$$

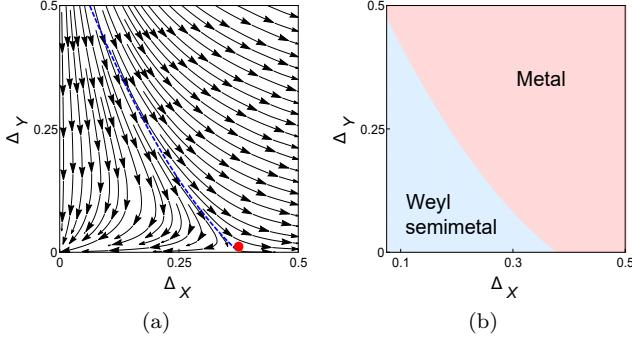


Figure 8: (a) The renormalization group flow diagram and (b) corresponding phase diagram in the  $\Delta_X - \Delta_Y$  plane, where  $X = V, A$  and  $Y = M, C$  obtained from Eq. (32). In these planes there is only one QCP at  $\Delta_X = 3\epsilon_m/8, \Delta_Y = 0$  (the red dot). The phase boundary between the Weyl semimetal and metal in panel (b) is determined by the irrelevant direction, shown by blue dotted line in panel (a).

Therefore, for the Gaussian white noise distribution, realized for  $\epsilon_m = 1$ , we obtain  $z = 3/2$  and  $\nu = 1$  from the leading order  $\epsilon_m$  expansion. If the bare value of either the chemical potential or axial potential disorder strength is zero, the quantum-critical behavior is governed by the QCP corresponding to the disorder of a nonvanishing bare value [41]. This QCP features the critical exponents of the same value to the one-loop order as in the case of the quantum-critical line, given by Eq. (34).

From the RG flow equations [see Eq. (32)], we find that both magnetic and current disorder are always *irrelevant* perturbations, at least to the leading order in the  $\epsilon_m$ -expansion. In the  $\Delta_X - \Delta_Y$  plane, where  $X = V, A$  and  $Y = M, C$  the RG flow diagram is shown in Fig. 8(a) and the corresponding phase diagram is shown in Fig. 8(b). Importantly, the QPT separating the metallic and the semimetallic phase in any  $\Delta_X - \Delta_Y$  plane is governed by the QCP located at  $\Delta_X = 3\epsilon_m/8$ . The phase boundary between these two phases is determined by the *irrelevant* direction at this QCP. Therefore, across the entire WSM-metal phase boundary in these planes the universality class of the QPT is identical and characterized by  $z = 1 + \epsilon_m/2$  and  $\nu^{-1} = \epsilon_m$ .

## B. $\epsilon_d$ expansion

The RG flow equations for the chiral symmetric disorder coupling constants within the framework of  $\epsilon_d$ -expansion are

$$\begin{aligned} \beta_{\Delta_V} &= \Delta_V [-\epsilon_d + 2F_+(\Delta_j)] + 8\Delta_M\Delta_C \\ \beta_{\Delta_A} &= \Delta_A [-\epsilon_d + 2F_+(\Delta_j)] + 4(\Delta_M^2 + \Delta_C^2) \\ \beta_{\Delta_M} &= \Delta_M \left[ -\epsilon_d + \frac{2}{3}F_-(\Delta_j) \right] + \frac{8}{3}(\Delta_C\Delta_V + \Delta_A\Delta_M) \end{aligned} \quad (35)$$

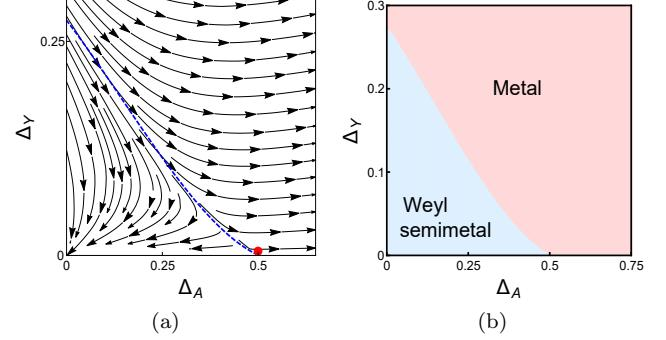


Figure 9: (a) The renormalization group flow diagram and (b) corresponding phase diagram in the  $\Delta_A - \Delta_Y$  plane, where  $Y = M, C$  obtained from  $\epsilon_d$  expansion for  $\epsilon_d = 1$ . There is only one quantum critical point at  $\Delta_A = \epsilon_d/2, \Delta_Y = 0$  (the red dot). The phase boundary between the Weyl semimetal and metal in panel (b) is determined by the irrelevant direction, shown by the blue dotted line in panel (a). These figures are qualitatively similar to the ones shown in Fig. 8, apart from the nonuniversal shift in the phase boundary.

$$\beta_{\Delta_C} = \Delta_C \left[ -\epsilon_d + \frac{2}{3}F_-(\Delta_j) \right] + \frac{8}{3}(\Delta_C\Delta_V + \Delta_A\Delta_M),$$

where  $F_{\pm}(\Delta_j) = (\Delta_V + \Delta_A) \pm (\Delta_C + \Delta_M)$ . These coupled flow equations also support only a line of QCPs in the  $\Delta_V - \Delta_A$  plane, as we previously found from Eq. (32) using  $\epsilon_m$ -expansion, now determined by

$$\Delta_{V,*} + \Delta_{A,*} = \frac{\epsilon_d}{2}, \quad (36)$$

similar to the one in Eq. (33). The critical exponents at each point of such line of QCPs is  $z = 1 + \epsilon_d/2$  and  $\nu^{-1} = \epsilon_d$ . Therefore, in three spatial dimensions  $\epsilon_d = 1$  and we find  $z = 3/2$  and  $\nu = 1$  [28, 39]. The RG flow diagram and the corresponding phase diagram are similar to the ones shown in Figs. 7(a) and 7(b). Only the location of the line of QCPs and the phase boundary shift in a nonuniversal fashion. The differences in the flow equations [ (33) and (35) ], arise from two diagrams shown in Fig. 4 (c) and (d), which produce ultraviolet divergent contributions, but only within the  $\epsilon_d$  expansion scheme. In the presence of only potential disorder we find  $z = 3/2$  and  $\nu = 1$  [28, 34, 35, 38, 39, 42].

Notice that if we start with only magnetic or current disorder, the axial disorder gets generated from Feynman diagrams (c) and (d) in Fig. 4. Thus, to close the RG flow equations, we need to account for  $\Delta_A$  coupling from the outset, and the resulting RG flow equations read

$$\begin{aligned} \beta_{\Delta_A} &= \Delta_A [-\epsilon_d + 2(\Delta_A + 3\Delta_Y)] + 4\Delta_Y^2 \\ \beta_{\Delta_Y} &= \Delta_Y \left[ -\epsilon_d + \frac{2}{3}(\Delta_Y - \Delta_A) \right] + \frac{8}{3}\Delta_A\Delta_Y, \end{aligned} \quad (37)$$

for  $Y = M, C$ . The above set of coupled RG flow equations supports only one QCP, located at  $\Delta_A = \epsilon_d/2, \Delta_Y = 0$ . The RG flow and the resulting phase

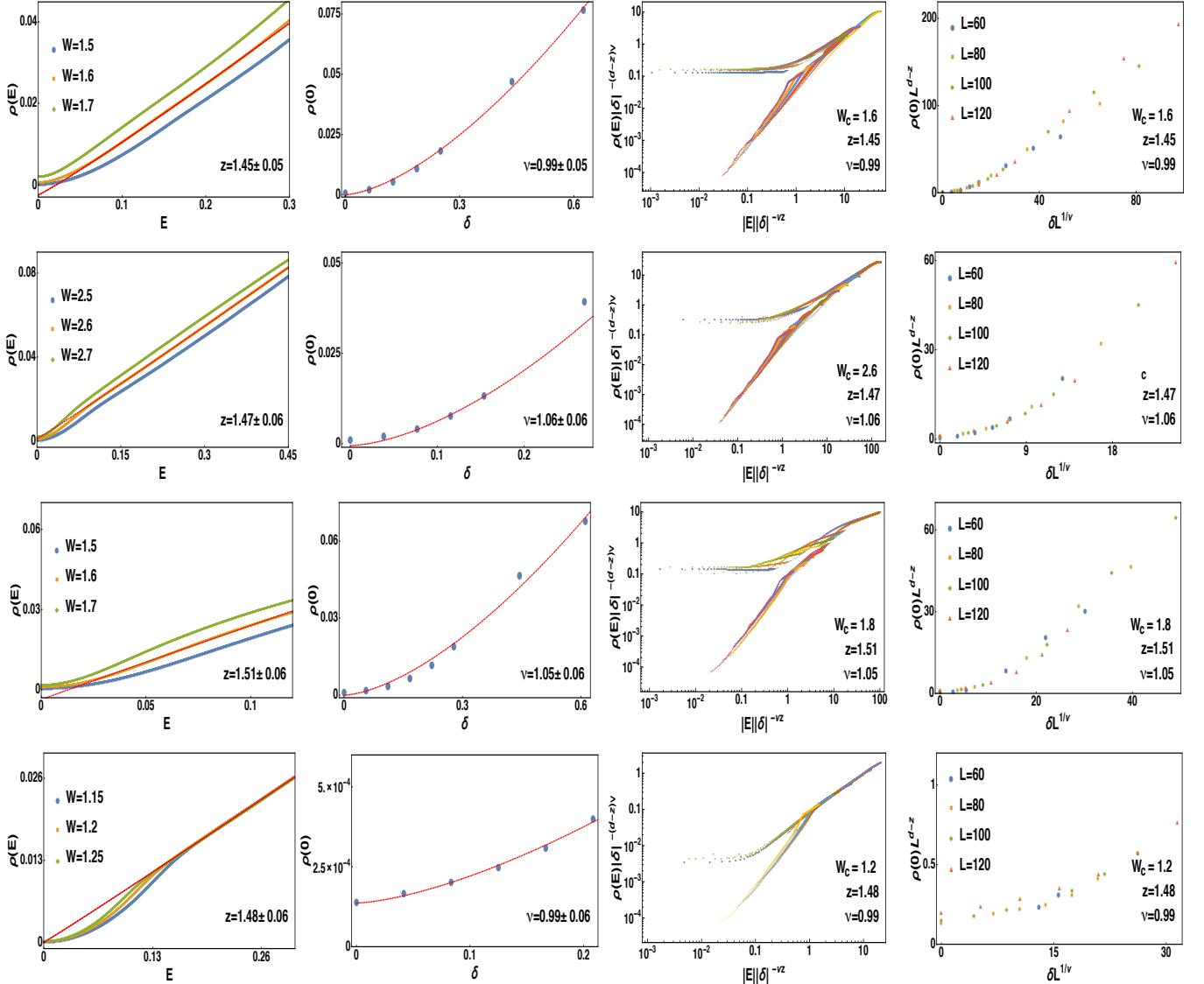


Figure 10: Scaling analysis of average density of states (ADOS) in various regimes of the phase diagram of a dirty WSM; plots from top to bottom rows correspond to potential, axial potential, axial current and current disorders. First column shows the scaling of ADOS  $\rho(E)$  vs.  $E$  around the critical strength of disorder ( $W = W_c$ ). The second column depicts the scaling of ADOS at zero energy  $\rho(0)$  vs.  $\delta$ , the reduced distance from the critical disorder defined as  $\delta = \frac{W-W_c}{W_c}$ . In the third column we display  $\rho(E)\delta^{-(d-z)\nu}$  vs.  $|E||\delta|^{-\nu z}$  for weak ( $W < W_c$ ) and strong ( $W > W_c$ ) disorder, and  $|E| \ll t (= 1)$ . All data collapse onto two branches. The top branch represents the metallic phase, while the lower one to WSM. Note that these two branches meet at large values of  $|E||\delta|^{-\nu z}$ , corresponding to the quantum critical regime. All data in first three columns are obtained from a system of linear dimension  $L = 120$ . The finite size data collapse inside the metallic phase is shown in the forth column, where we compare  $\rho(0)L^{d-z}$  vs.  $\delta L^{1/\nu}$  for  $60 \leq L \leq 120$ . Notice that all data collapse onto one branch for small to moderate values of  $\delta L^{1/\nu}$ , with the numerically extracted values of the critical exponents  $z$  and  $\nu$ , quoted in the figure and summarized in Table I. Scaling of ADOS and data analysis is discussed in details in Sec. VI. In a certain lattice model axial current disorder also correspond to magnetic impurities, see Table II.

diagrams are shown in Figs. 9(a) and 9(b), respectively. Hence, in the presence of magnetic and current disorder the transition to the metallic phase is controlled by the QCP due to axial disorder. If we also take into account the presence of potential disorder, then such a semimetal-metal QPT takes place through one of the points residing

on the line of QCPs in the  $\Delta_V - \Delta_A$  plane, depending on the bare relative strength of these two disorder couplings.

### C. Chiral superuniversality

From the discussion in previous two subsections, we can conclude that in the presence of chiral-symmetric disorder in a WSM, the semimetal-metal QPT takes place either through a QCP or a line of QCPs. The location of the line of QCPs and the resulting phase boundaries are nonuniversal and thus dependent on the RG scheme. However, the quantum critical behavior with chiral symmetric disorder couplings is insensitive of these details, at least to the leading order in the expansion parameter, and all QPTs in the four-dimensional hyperplane of disorder coupling constants, are characterized by identical set of critical exponents, namely  $z = 1 + \epsilon/2$  and  $\nu^{-1} = \epsilon$ , with  $\epsilon = 1$ . Therefore, emergent quantum critical behavior for strong chiral-symmetric disorder stands as a rare example of superuniversality, and we name it *chiral superuniversality*. Next we demonstrate emerging of such superuniversality across WSM-metal QPT by *numerically* analyzing the scaling of average DOS in the presence of generic chiral symmetric disorder.

## VI. NUMERICAL DEMONSTRATION OF CHIRAL SUPERUNIVERSALITY

Motivated by the field-theoretic prediction of emergent chiral superuniversality across the WSM-metal QPTs driven by CSP disorder, next we numerically investigate the scaling of average DOS across such QPTs. Since  $\varrho(0)$  vanishes and is finite in the WSM and metallic phases, respectively, it can be promoted as a bonafide order-parameter across the WSM-metal QPT [49, 51, 53, 54, 56, 60]. In addition, such analysis endows an opportunity to extract the critical exponents for the transition non-perturbatively and, at the same time, test the validity of the proposed scenario for chiral superuniversality. The WSM phase is realized from the tight-binding model, defined through Eqs. (3) and (5), which we implement on a cubic lattice of linear dimension  $L$ . For numerical analysis we set  $m_z = 0$ ,  $t = 1 = t_0$  and  $t_z = \frac{1}{2}$  in the clean model, given by Eq. (2)-(5). We use lattice realizations of disorder introduced in Appendix D. We impose periodic boundary condition in all three directions. The average DOS is computed by using the *kernel polynomial method* [68]. The average is taken over 20 random realization of disorder that minimizes the residual statistical error in average DOS, which is a self-averaged quantity. We typically compute 4096 Chebyshev moments and take trace over  $\sim 12$  random vectors to compute average DOS. All types of disorder are distributed uniformly and randomly within the range  $[-W, W]$ . The scaling of average DOS can be derived in the following way.

Note that total number of states  $N(E, L)$  in a  $d$ -dimensional system of linear dimension  $L$ , below the energy  $E$  is proportional to  $L^d$ , and in general is a function of two dimensionless parameters  $L/\xi$  and  $E/E_0$ . Here,

$\xi \sim \delta^{-\nu}$  is the correlation length that diverges at the QCP, located at  $\delta = 0$ , where  $\delta = \frac{W-W_c}{W_c}$  is the reduced distance from the QCP at  $W = W_c$ . Consequently, the correlation energy, defined as  $E_0 \sim \delta^{\nu z}$  vanishes as the QCP is approached from either side of the transition [74]. Following the standard formalism of scaling theory we then can write

$$N(E, L) = \left( \frac{L}{\xi} \right)^d G \left( \frac{E}{\delta^{\nu z}}, \frac{L}{\delta^{-\nu}} \right), \quad (38)$$

where  $G$  is an universal but unknown scaling function. Therefore, from the definition of average DOS  $\varrho(E, L) = L^{-d} dN(E, L)/dE$  we arrive at the following scaling form

$$\varrho(E, L) = \delta^{\nu(d-z)} F \left( |E| \delta^{-\nu z}, \delta L^{1/\nu} \right), \quad (39)$$

where  $F$  is yet another universal, but typically unknown scaling function. However, we can access the behavior of the scaling function in different regimes of the phase diagram of a dirty WSM, which we exploit to compute critical exponents characterizing the transition. In the final step we have used the fact that average DOS remains particle-hole symmetric, but on average.

Let us first focus on the quantum critical regime and for now we assume that the system size is sufficiently large that we can neglect the  $L$ -dependence in Eq. (39). In this regime the scaling function must be independent of  $\delta$ , dictating  $F(x) \sim x^{\frac{d}{z}-1}$ . Therefore, when  $W = W_c$  we compare  $\varrho(E)$  vs.  $E^{\frac{d}{z}-1}$  and extract the DSE  $z$ . Such analysis for all four possible CSP disorders is shown in the first column of Fig. 10 and numerically extracted values of  $z$  are quoted in Table I. Within the numerical accuracy, we always find  $z \approx 1.5$  in excellent agreement with the field-theoretic result, obtained from the leading order  $\epsilon$  expansions.

Next we proceed to the metallic side of the transition, where average DOS at zero energy becomes finite. From the scaling function in Eq. (39), we obtain  $\varrho(0) \sim \delta^{(d-z)\nu}$ . Thus by comparing  $\varrho(0)$  vs.  $\delta$ , we extract the CLE  $\nu$ , using already obtained value of the DSE  $z$ , as shown in the second column of Fig. 10. The numerically found CLE is also quoted in Table I, and within numerical accuracy  $\nu \approx 1$  always, irrespective of the nature of CSP disorder. Once again we find an excellent agreement of numerically extracted values of  $\nu$  with the one obtained from the leading order  $\epsilon$ -expansions. These two results strongly support the picture of chiral superuniversality.

To test the quality of our numerical analysis we search for two types of data collapse. First, we compare  $\varrho(E)|\delta|^{-\nu(d-z)}$  vs.  $|\delta|^{-\nu z}|E|$ , motivated by the scaling form of average DOS, displayed in Eq. (39). Using numerically obtained values of  $\nu$  and  $z$ , we find that for energies much smaller than the bandwidth ( $|E| \ll 1$ ), all data collapse onto two separate branches for all four disorders, as shown in the third column of Fig. 10. While the top branch corresponds to the metallic phase, the lower one stems from the WSM phase and eventually these two branches meet in the quantum critical regime.

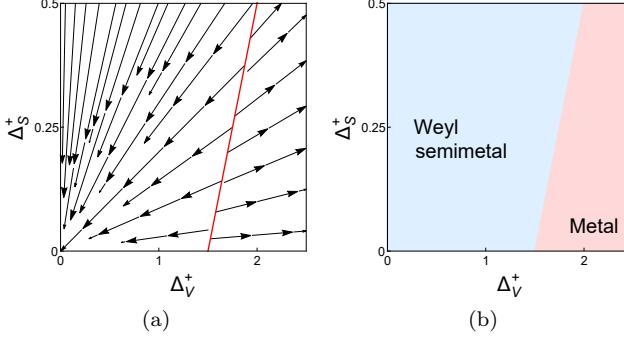


Figure 11: (a) The RG flow diagram and (b) corresponding phase diagram in the  $\Delta_V^+ - \Delta_S^+$  plane obtained from  $\epsilon_m$  expansion for  $\epsilon_m = 1$ . The WSM-metal QPT in this coupling constant space is controlled by the line of QCPs [see Eq. (42)], shown by the red line in panel (a) that in turn also determines the phase boundary between these two phases, as shown in panel (b).

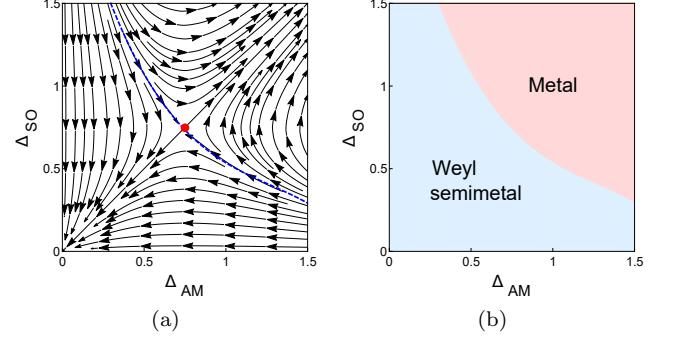


Figure 12: (a) The renormalization group flow diagram and (b) corresponding phase diagram in the  $\Delta_{AM} - \Delta_{SO}$  plane obtained from  $\epsilon_m$  expansion for  $\epsilon_m = 1$ . There is only one quantum critical point at  $\Delta_{AM} = \Delta_{SO} = 3\epsilon_m/4$  (the red dot). The phase boundary between the Weyl semimetal and metal in panel (b) is determined by the irrelevant direction, shown by blue dotted line in panel (a).

Finally, we demonstrate a finite size data collapse for  $\varrho(0)$  for different system sizes by focusing on the metallic side of the transition. Setting  $E = 0$  in Eq. (39), we obtain  $\varrho(0) = L^{z-d} F(0, \delta L^{1/\nu})$ . Hence, we compare  $\varrho(0) L^{d-z}$  vs.  $\delta L^{1/\nu}$  and find an excellent data collapse for  $60 < L < 120$ , using numerically obtained values of  $\nu$  and  $z$  for all four disorders, as shown in the fourth column of Fig. 10. The data collapse becomes systematically worse for large values of  $\delta$  or stronger disorder due to the existence of a second transition that takes the system from a metallic phase to an Anderson insulator. Therefore, our thorough numerical analysis provides a valuable and unprecedented insight into the nature of the WSM-metal QPTs driven by generic chiral symmetric disorder, and supports the proposal of emergent chiral superuniversality across such QPTs.

## VII. CHIRAL SYMMETRY BREAKING DISORDER

In a WSM constituted by a single pair of Weyl nodes, there are four CSB disorders, namely temporal and spatial components of a tensor disorder, which in a suitable lattice model respectively represents spin-orbit and axial magnetic disorder, as well as scalar and pseudoscalar mass disorder, see Table II. Once again we will address the effects of weak and strong CSB disorder by using both  $\epsilon_m$  and  $\epsilon_d$  expansions.

### A. $\epsilon_m$ expansion

Within the framework of an  $\epsilon_m$  expansion the RG flow equations to one-loop order read as

$$\begin{aligned} \beta_{\Delta_{SO}} &= \Delta_{SO} \left[ -\epsilon_m + \frac{4}{3} (\Delta_{AM} - \Delta_S) \right], \\ \beta_{\Delta_{AM}} &= \Delta_{AM} \left[ -\epsilon_m + \frac{4}{3} (\Delta_{SO} - \Delta_P) \right], \\ \beta_{\Delta_S} &= \Delta_S \left[ -\epsilon_m + \frac{4}{3} (5\Delta_{SO} - 4\Delta_{AM} - 2\Delta_S + \Delta_{PS}) \right], \\ \beta_{\Delta_{PS}} &= \Delta_{PS} \left[ -\epsilon_m + \frac{4}{3} (5\Delta_{AM} - 4\Delta_{SO} - 2\Delta_{PS} + \Delta_S) \right]. \end{aligned} \quad (40)$$

Therefore, individually each CSB disorder is always an irrelevant perturbation, at least to the leading order in the  $\epsilon_m$  expansion, and as such does not lead to any QPTs. However, in the absence of chiral symmetry all four disorder couplings are present and to address the critical properties in this situation we recast the above flow equations in terms of newly defined coupling constants as

$$\begin{aligned} \beta_{\Delta_V^+} &= -\epsilon_m \Delta_V^+ + \frac{2}{3} \left[ (g_V^+)^2 - (\Delta_V^-)^2 - \Delta_V^+ \Delta_S^+ - \Delta_V^- \Delta_S^- \right] \\ \beta_{\Delta_V^-} &= -\epsilon_m \Delta_V^- - \frac{2}{3} \left[ \Delta_V^- \Delta_S^+ + \Delta_V^+ \Delta_S^- \right] \\ \beta_{\Delta_S^+} &= -\epsilon_m \Delta_S^+ - \frac{2}{3} \left[ (\Delta_S^+)^2 + 3(\Delta_S^-)^2 - \Delta_V^+ \Delta_S^+ - 9\Delta_V^- \Delta_S^- \right] \\ \beta_{\Delta_S^-} &= -\epsilon_m \Delta_S^- - \frac{2}{3} \left[ \Delta_S^- \Delta_V^+ - 4\Delta_S^+ \Delta_S^- - 9\Delta_S^+ \Delta_V^- \right], \end{aligned} \quad (41)$$

where  $\Delta_V^\pm = \Delta_{SO} \pm \Delta_{AM}$ ,  $\Delta_S^\pm = \Delta_S \pm \Delta_{PS}$ . The above set of RG flow equations supports a line of QCPs determined by the equation

$$\Delta_{V,*}^+ = \Delta_{S,*}^+ + \frac{3\epsilon_m}{2}, \quad \Delta_{V,*}^- = 0, \quad \Delta_{S,*}^- = 0. \quad (42)$$

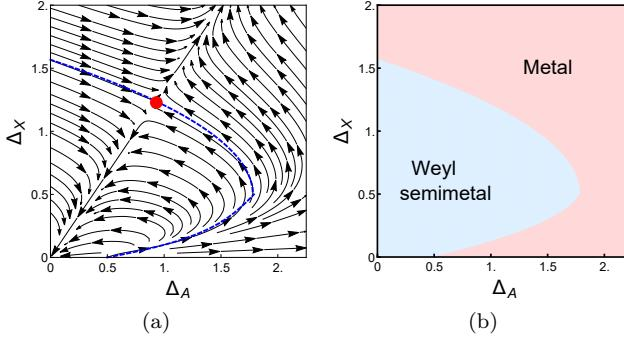


Figure 13: (a) The RG flow diagram and (b) corresponding phase diagram in the  $\Delta_A - \Delta_X$  plane obtained from  $\epsilon_d$  expansion for  $\epsilon_d = 1$ , where  $X = SO, AM$ . There exists only one QCP at  $\Delta_A = 6\epsilon_d/5$ ,  $\Delta_X = 9\epsilon_d/10$ . The QCP at  $\Delta_A = \epsilon_d/2$  in the absence of a CSB disorder now possesses two unstable directions. A new critical point emerges from the competition between the chiral and non-chiral disorder [28, 39].

Notice that if we tune the CSB disorders, so that  $\Delta_V^- = \Delta_S^- = 0$ , these two coupling constants do not get generated through quantum corrections, and the plane with  $\Delta_V^- = \Delta_S^- = 0$ , shown in Fig. 11, remains invariant under the RG. The RG flow in this plane is shown in Fig. 11(a), and the corresponding phase diagram is presented in Fig. 11(b). The WSM-metal phase boundary in the  $\Delta_V^+ - \Delta_S^+$  plane is determined by the line of QCPs, given by Eq. (42), qualitatively similar to the situation in the presence of potential and axial disorders, as shown in Fig. 7. However, these two scenarios are fundamentally different in the sense that while the DSE  $z = 1 + \epsilon/2$ , with  $\epsilon = \epsilon_m$  or  $\epsilon_d$ , is fixed along the entire line of QCPs in the  $\Delta_V - \Delta_A$  plane, it varies continuously along the line of QCPs in the  $\Delta_V^+ - \Delta_S^-$  plane according to

$$z = 1 + \frac{2}{3} \left[ 5\Delta_{V,*}^+ + \Delta_{S,*}^+ \right] = 1 + 5\epsilon_m + 4\Delta_{S,*}^+, \quad (43)$$

where the quantity with subscript “\*” denote the critical value for WSM-metal transition. Such continuously varying DSE leaves its signature in critical scaling of various physical observables, as we discuss below, and qualitatively mimics the picture of Kosterlitz-Thouless transition. Notice that the end point of such line of QCPs on the  $\Delta_V^+$  axis reside in the  $\Delta_{SO} - \Delta_{AM}$  plane at  $\Delta_{SO} = \Delta_{AM} = 3\epsilon_m/4$ , and the RG flow in this plane is shown in Fig. 12(a). The phase diagram of a dirty WSM containing only spin-orbit and axial magnetic disorder in this plane is shown in Fig. 12(b), with  $z = 1 + 5\epsilon_m$ , which is directly obtained from Eq. (43) by setting  $\Delta_S^+ = 0$ . It is worth pointing out that in the  $\Delta_{SO} - \Delta_{AM}$  plane the phase boundary between the WSM and metallic phase is set by the irrelevant parameter associated with the QCP, while when such QCP percolates through  $\Delta_V^+ - \Delta_S^+$  plane in the form of a line of QCPs, it is determined by the relevant direction at each point on the line of QCPs.

## B. $\epsilon_d$ expansion

Next address the effects of CSB disorder within the framework of an  $\epsilon_d$  expansion. In this method the RG flow equations become very complicated due to the ultraviolet divergent contribution arising from the class of the Feynman diagrams shown in Fig. 4 (c) and (d), and it is challenging to decode the emergent quantum-critical phenomena. Thus we attempt to unearth critical properties by focusing on various coupling constant subspaces that remain closed under the RG, at least to the leading order. Let us first focus on spin-orbit or axial magnetic disorder. The RG flow equations read

$$\begin{aligned} \beta_{\Delta_X} &= -\epsilon_d \Delta_X - \frac{2}{3} \Delta_X^2 + 2\Delta_X \Delta_A \\ \beta_{\Delta_A} &= -\epsilon_d \Delta_A + 2\Delta_A^2 - 6\Delta_A \Delta_X + 4\Delta_X^2, \end{aligned} \quad (44)$$

where  $X = SO, AM$ . Notice that even though the bare theory contains only spin-orbit or axial magnetic disorders, the CSP axial disorder gets generated and in order to keep the RG flow equations closed we need to include the latter from the outset. The coupled flow equations support one QCP, located at  $\Delta_X = 9\epsilon_d/10$ ,  $\Delta_A = 6\epsilon_d/5$  [28, 39]. The RG flow diagram is shown in Fig. 13(a), and the resulting phase diagram is displayed in Fig. 13(b). Note that QCP obtained in the absence of the CSB disorders, located at  $\Delta_A = \epsilon_d/2$  now becomes unstable in the presence of either spin-orbit or axial magnetic disorder, and a new QCP results from the competition between these two disorders, as mentioned above. This outcome although bears contrast with our previously reported results obtained from  $\epsilon_m$  expansion, still shows some qualitative similarities, as we argue below. Notice that the DSE and CLE at the new QCP, shown in Fig. 13(a), are respectively given by

$$z = 1 + \frac{9}{2}\epsilon_d, \quad \nu^{-1} = \epsilon_d. \quad (45)$$

As a result the mean DOS at the QCP diverges as  $\varrho(E) \sim |E|^{-5/11}$  for  $\epsilon_d = 1$  or  $d = 3$ , since  $z > d$ . [for scaling theory of average DOS consult Sec. VIII]. Hence, both  $\epsilon$ -expansions give rise to diverging DOS at the QCP controlled via spin orbit and axial magnetic disorder. Although the calculated values of DSE depend on RG scheme, to the leading order they do not differ significantly,  $z = 6$  for  $\epsilon_m = 1$ , and  $z = 11/2$  for  $\epsilon_d = 1$ , while  $\nu = 1$ , is independent of RG scheme.

## C. Mass disorder

We now discuss the role of mass disorder in WSMs. It should be noted that a WSM can be susceptible to two different types of mass disorder (a) scalar mass disorder and (b) pseudo-scalar mass disorder. Both of them break the chiral symmetry, but can be rotated into each other by the generator of the chiral symmetry  $\gamma_5$ . The flow

equation for mass disorder within the framework of an  $\epsilon$  expansion reads as

$$\beta_{\Delta_X} = -\epsilon_j \Delta_X - \alpha_j \Delta_X^2, \quad (46)$$

for  $X = S, PS$ ,  $\alpha_m = 8/3$  and  $\alpha_d = 2$ ,  $j = m, d$  corresponds to  $\epsilon_m$  and  $\epsilon_d$  expansions, respectively. Hence, by itself scalar or pseudoscalar mass disorder does not drive any WSM-metal QCP, at least within the leading order in  $\epsilon$ -expansions. In this regard both  $\epsilon_m$  and  $\epsilon_d$  expansions yield an identical result.

Finally, we discuss yet another interesting aspect of mass disorder, when it coexists with the axial one. The flow equations in the presence of these two disorders are

$$\beta_{\Delta_A} = -\epsilon_j \Delta_A + \tilde{\alpha}_j \Delta_A \Delta_-, \quad \beta_{\Delta_X} = -\epsilon_j \Delta_X - \tilde{\alpha}_j \Delta_X \Delta_- \quad (47)$$

for  $X = S, PS$ , where  $\Delta_- = \Delta_A - \Delta_X$ ,  $\tilde{\alpha}_m = 8/3$ ,  $\tilde{\alpha}_d = 2$ , and respectively  $j = m, d$  corresponds to  $\epsilon_m$  and  $\epsilon_d$  expansions. These two flow equations supports a line of QCPs, determined by

$$\Delta_{A,*} = \frac{\epsilon_j}{\tilde{\alpha}_j} + 2\Delta_{X,*}. \quad (48)$$

The location of such line of QCPs is regularization dependent (through  $\tilde{\alpha}_j$ ), along which the DSE and CLE, given by

$$z = 1 + \frac{\epsilon_j}{2} + 2\Delta_{S,*}, \quad \nu^{-1} = \epsilon_j \quad (49)$$

are identical in both  $\epsilon$ -expansion schemes. Therefore, in a WSM with these two disorders the DSE continuously increases from  $z = 3/2$  in an unbounded fashion, while the CLE remains fixed. The numerical investigation of such interesting possibility is left for a future work.

### VIII. QUANTUM CRITICAL SCALING OF PHYSICAL OBSERVABLES

As demonstrated in the previous two sections QPT from a WSM to a diffusive metal can be driven by different types of elastic scatters, and the critical exponents are remarkably dependent on the actual nature of randomness. We here highlight how these exponents can affect the scaling behavior of measurable quantities as the Weyl material undergoes this QPT.

• *Residue of quasiparticle pole:* As the WSM-metal QCP is approached from the semimetallic phase, the residue of quasiparticle pole vanishes and beyond the critical strength of disorder Weyl fermions cease to exist as sharp quasiparticle excitations, similar to the situation for Dirac fermion-Mott insulator QPT in the presence of a strong Hubbard interaction [75, 76]. The residue of quasiparticle pole ( $Z$ ) vanishes according to

$$Z \sim \left( \frac{\Delta_* - \Delta}{\Delta_*} \right)^{\nu \eta_\Psi} \equiv \delta^{\nu \eta_\Psi}, \quad (50)$$

where  $\eta_\Psi$  is the fermionic anomalous dimension at the critical point located at the disorder strength  $\Delta = \Delta_*$ . Within the framework of an  $\epsilon_d$  expansion  $\eta_\Psi = 0$  to the leading order in  $\epsilon_d$ , and one needs to account for two-loop diagrams to obtain finite  $\eta_\Psi$ . In contrast, in the  $\epsilon_m$  expansion we obtain nontrivial fermionic anomalous dimension even to the one-loop order, and  $\eta_\Psi \sim \epsilon$ , as shown in Eq. (24). Therefore, at the WSM-metal QCP, the quasiparticle spectrum displays *branch-cut* and the critical point represents a strongly coupled *non-Fermi liquid*. Alternatively, the residue of quasiparticle pole plays the role of a *bona fide* order parameter in the semimetallic side. It is worth mentioning that the disappearance of residue of quasiparticle pole has recently been tracked in quantum Monte Carlo simulations for Hubbard model in two-dimensional honeycomb lattice [76], and we can expect that future numerical work can verify our proposed scaling form in Eq. (50) across the disorder driven WSM-metal QPTs. The Fermi velocity scales as  $v \sim |\delta|^{\nu(z-1)}$ , and since  $z > 1$  at the QCP or the quantum-critical line, the Fermi velocity vanishes at the transition to the metallic phase.

• *Average density of states:* The most widely studied physical quantity in numerical simulations across the WSM-metal QPT is the average DOS [49, 51, 53, 54, 56, 60]. We can infer the scaling form of the average DOS in the thermodynamic limit  $L \rightarrow \infty$  in different phases by using its scaling function (39). In the quantum critical regime  $\varrho(E)$  should be independent of  $\delta$ , yielding  $\varrho_Q(E) \sim E^{d/z-1}$ . Inside the WSM phase, the average DOS scales as  $\varrho_W(E) \sim \delta^{(1-z)\nu} |E|^2$ . In the metallic phase average DOS at zero energy is finite and scales as  $\varrho(0) \sim \delta^{(d-z)\nu}$ . From the quoted values of DSE and CLE, it is straightforward to find the scaling of average DOS in these three regimes of the phase diagram in a dirty WSM. We point out that the scaling of average DOS behaves differently in the quantum critical regime depending on the actual nature of the disorder driving the transition. In the presence of chiral symmetric disorder couplings, the dynamic scaling exponent is  $z = 3/2$ , yielding  $\varrho_Q(E) \sim |E|$ . On the other hand, when the WSM-metal QPT is driven by CSB disorder, we always find that  $z > d$ , although the actual value of  $z$  turns out to be (marginally) regularization-dependent. Therefore, the average DOS inside the quantum critical regime  $\varrho_Q(E)$  is expected to *diverge* when the WSM-metal QPT is driven purely by CSB disorder. In contrast, the DSE varies continuously when the WSM-metal QPT is driven by the simultaneous presence of strong mass and axial disorders, and  $z$  increases continuously as the mass disorder gets stronger. Hence, with increasing strength of mass disorder,  $\varrho(E)$  crosses over from vanishing to diverging scaling as  $E \rightarrow 0$ . We therefore predict a different behavior of average DOS in the presence of the disorder transforming distinctly under the chiral symmetry which should be testable in lattice based numerical calculations.

• *Conductivity:* The optical conductivity ( $\sigma$ ) at  $T = 0$  can as well serve as an order parameter across the WSM-

metal QPT, and assumes the following scaling ansatz for frequency ( $\Omega$ ) much smaller than the bandwidth [40]

$$\sigma(\Omega) = \delta^{\nu(d-2)} \mathcal{G}(\Omega \delta^{-\nu z}), \quad (51)$$

where  $\mathcal{G}$  is yet another unknown universal scaling function. This scaling form remains operative even at finite temperature as long as  $\Omega \gg T$ , i.e., in the *collisionless* regime. In the *collision dominated* regime at  $T \gg \Omega$ , the dc conductivity also assumes a similar scaling form as in Eq. (51), upon replacing the frequency ( $\Omega$ ) by temperature ( $T$ ) [35, 50, 77]. In the WSM side of the transition, the OC vanishes linearly with  $\Omega$  and scales as  $\sigma_W(\Omega) \sim \delta^{\nu(1-z)(d-2)} \Omega^{d-2}$ . Inside the critical regime the OC scales as  $\sigma_Q(\Omega) \sim \Omega^{(d-2)/z}$ . Since in the presence of strong CSP disorder  $z = 3/2$ , the optical conductivity inside the quantum critical regime vanishes as  $\sigma_Q(\Omega) \sim \Omega^{2/3}$ . Since for non-chiral disorder the DSE is typically much bigger than in the presence of chiral symmetric one, the optical conductivity vanishes with a *weaker* power as  $\Omega \rightarrow 0$  when the WSM-metal QPT is driven by former disorder. Hence, inside the weakly disordered WSM phase and the quantum critical regime, the system becomes *more metallic* in the presence of CSB disorder. Inside the metallic phase, the optical conductivity becomes finite and scales as  $\sigma_M(0) \sim \delta^{\nu(d-2)}$  as  $\Omega \rightarrow 0$ . Within the leading order  $\epsilon_m$  or  $\epsilon_d$  expansions, the conductivity of the metal is therefore independent of the actual nature of elastic scatterers, since  $\nu^{-1} = \epsilon_m$  or  $\epsilon_d$ , and  $\epsilon_m = 1$ ,  $\epsilon_d = 1$ .

• *Specific heat*: The specific heat ( $C_v$ ) also displays distinct scaling behavior in three regimes of the phase diagram of a dirty WSM. The scaling of specific heat at temperature much smaller than bandwidth follows the ansatz [34]

$$C_V(T) = \frac{T^{d/z}}{v^d} \mathcal{H}(T \delta^{-\nu z}), \quad (52)$$

where  $\mathcal{H}$  is also an unknown universal scaling function. In the WSM phase,  $\mathcal{H}(x) \sim x^{d(z-1)/z}$  and the specific heat scales as  $C_V \sim \delta^{\nu(1-z)} T^d$ , so that we recover  $T^3$  dependence for three dimensional Weyl fermion. Inside the metallic phase,  $\mathcal{H}(x) \sim x^{1-d/z}$ , yielding  $C_V \sim \delta^{\nu(d-z)} T$  and we obtain  $T$ -linear specific heat, similar to the situation in Fermi liquids. By contrast, inside the critical regime  $\mathcal{H}(x) \sim x^0$ , yielding  $C_V \sim T^{3/z}$ . Therefore, for different classes of disorder, the specific heat displays distinct power-law dependence on temperature inside the quantum critical regime, while its scaling inside the WSM and metallic phases is insensitive to the nature of random impurities. Hence, the scaling of specific heat inside the critical regime can indicate the nature of the dominant source of elastic scattering, and can also be used to extract the extent of the critical regime and crossover boundaries among different phases of a dirty Weyl system at finite temperature [53].

• *Mean-free path*: The quasiparticle mean-free path ( $\mathcal{L}$ ) also follows the critical scaling

$$[\mathcal{L}(E)]^{-1} = \delta^\nu \mathcal{J}(E \delta^{-\nu z}), \quad (53)$$

where  $\mathcal{J}$  is a universal, but unknown scaling function, with energy much smaller than bandwidth. At the QCP ( $\delta = 0$ ) the mean-free path should be independent of  $\delta$ , implying  $\mathcal{J}(x) \sim x^{-1/z}$ . Therefore, inside the quantum critical fan, the mean-free path at zero energy diverges as  $\mathcal{L}(E) \sim E^{-1/z}$ . In the metallic phase,  $\mathcal{J}(x) \sim x^0$  as  $x \rightarrow 0$ , leading to finite mean-free path at zero energy, and  $\mathcal{L}(0) \sim \delta^{-\nu}$ . On the other hand, in the WSM phase, the mean-free path  $\mathcal{L}_W(E) \sim \delta^{\nu(z-1)} E^{-1}$ , as  $E \rightarrow 0$ . Since at all disorder driven QCPs  $z > 1$ ,  $\mathcal{L}_W(E)$  decreases with increasing disorder, indicating propensity toward the onset of a metallicity in the system. In particular in the presence of CSB disorders the system approaches the metallic phase faster.

• *Grüneisen parameter*: Yet another directly measurable quantity is the Grüneisen parameter, defined as  $\gamma = \alpha/C_P$ , where  $\alpha$  is the thermal expansion parameter, and  $C_P$  is the specific heat measured at constant pressure. The Grüneisen ratio in the WSM phase  $\gamma_W \sim T^{-4}$ , while inside the critical regime  $\gamma_Q \sim T^{-(1+d/z)}$ . Inside the metallic phase  $\gamma_M \sim T^{-2}$ . Therefore, the Grüneisen parameter displays distinct power law behavior in three different phases of a dirty WSM.

Fascinating scaling behavior can also be observed for the magnetic Grüneisen ratio, defined as  $\Gamma_H = (\partial M/\partial T)_H/C_H$ , where  $M \propto H$  is magnetization,  $C_H$  is the molar specific heat, and  $H$  is the magnetic field strength. In the presence of sufficiently weak randomness when Landau quantization is sharp ( $\omega_c \tau \gg 1$ , where  $\omega_c$  is cyclotron frequency and  $\tau$  is scattering lifetime) and dominates over the Zeeman coupling, leading to  $\Gamma_H \sim T^{-4/z}$ . On the other hand, in the presence of strong elastic scattering when  $\omega_c \tau \ll 1$  the Landau levels are sufficiently broadened and the dominant energy scale is set by Zeeman coupling, yielding  $\Gamma_H \sim T^{-2}$ , which is independent of dimensionality ( $d$ ) or DSE ( $z$ ). Therefore, for a fixed weak magnetic field, as the strength of impurities is gradually increased, the magnetic Grüneisen ratio should display a smooth crossover from  $T^{-4}$  to  $T^{-2}$  dependence. Note that such a crossover will take place even before the system enters the quantum critical regime and will persist in the metallic regime as well, since elastic scattering is strong in these two phases.

## IX. SUMMARY AND DISCUSSION

In this paper we have studied the role of generic disorder in a Weyl semimetal, by considering its simplest realization, comprised of only two Weyl nodes. When the system resides in the proximity of semimetal-insulator quantum phase transition, the generalized Harris criterion suggests that such critical point is stable in the presence of weak but generic disorder. By contrast, a multicritical point appears in the phase diagram for strong disorder, where the Weyl semimetal, insulator and a metallic phase meet. Within the framework of an appropri-

ate  $\epsilon$ -expansion we show that the critical exponents at such multicritical point are (i) dynamic scaling exponent  $z = 1 + \epsilon_n/2$ , and (ii) correlation length exponent  $\nu = 1/\epsilon_n$  that controls the relevance of disorder coupling, where  $\epsilon_n = 1/2$  for physical system.

On the other hand, when the system is deep inside the Weyl semimetal phase, we have shown that the continuous global chiral  $U(1)$  symmetry plays a fundamental rule in classifying the disorder-driven Weyl semimetal-metal quantum phase transitions. The simplest realization of a Weyl semimetal is susceptible to eight types of disorder, among which only four preserve such chiral symmetry. Using two different  $\epsilon$ -expansions, we have shown that the chiral symmetric disorder driven semimetal-metal transition takes place through either a quantum critical point or a line of quantum critical points. Irrespective of details, the critical exponents are always  $z = 1 + \epsilon/2$  and  $\nu = \epsilon^{-1}$ , and  $\epsilon = 1$  corresponds to the physical situation. Such unique set of exponents in the presence of generic chiral symmetric disorder gives birth to an *emergent chiral superuniversality* across the Weyl semimetal-metal quantum phase transition.

Furthermore, we have performed a thorough numerical analysis of average density of states in Weyl semimetals with chiral symmetric disorder. The emergence of chiral superuniversality has been demonstrated through numerical analysis of average density of states near zero energy. We show that for any such disorder Weyl semimetal undergoes a continuous quantum phase transition into a diffusive metallic phase. Within the numerical accuracy, we find that across the transition  $z \approx 1.5$  and  $\nu \approx 1$ , in excellent agreement with our field theoretic predictions obtained from leading order  $\epsilon$ -expansions (see Table I for comparison). The quality as well as reliability of our numerical analysis has been anchored through completely different types of high-quality data collapses, shown in Fig. 10, in the entire phase diagram of a dirty Weyl semimetal for all possible chiral disorder.

For chiral symmetry breaking disorder, the Weyl semimetal-metal quantum phase transition also takes place through a critical point or a line of critical points, but the critical exponents are significantly different from the ones reported in the presence of chiral disorder. Even though the critical exponents across such semimetal-metal transition turn out to be dependent on the renormalization group scheme, we always find  $z > d$  and  $\nu = 1/\epsilon$  from leading order  $\epsilon$ -expansions. Therefore, metallicity sets in much faster in the system, yielding *diverging* average density of states at the quantum critical point in this case. Numerical demonstration of such outcomes is, however, left for a future investigation.

Most strikingly, irrespective of the details of the  $\epsilon$ -expansions, all possible semimetal-metal quantum phase transitions can be classified according to the transformation of disorder under the emergent continuous chiral symmetry. Even though we promoted such classification scheme in a Weyl semimetal with only two nodes, our prescription can easily be generalized to Weyl systems with

multiple flavors, as well as topological Dirac semimetals with bona fide time-reversal symmetry that has recently been found in  $\text{Cd}_2\text{As}_3$  [78] and  $\text{Na}_3\text{Bi}$  [79] and the one found at the quantum critical point residing between two topologically distinct insulating vacua.

We here mention that  $\epsilon_d$  expansion can be problematic beyond the leading order in  $\epsilon_d$ , since the contribution from diagrams (c) and (d) in Fig. 4 and their higher-loop cousins are typically ultraviolet divergent and one loses the order by order control over the perturbative calculation [38, 42]. Such a class of diagrams is, however, ultraviolet finite and thus does not contribute to renormalization group flow equations in the  $\epsilon_m$  expansion scheme. We therefore strongly believe that higher order perturbation theory can only be reliable in the  $\epsilon_m$  expansion scheme, and our results can serve as an ideal testbed to investigate the reliability of these two schemes.

Finally we comment on some non-perturbative effects of disorder in Weyl semimetals, such as puddles [80], Lishitz tail [81], and rare-region states and Griffiths physics [32, 58]. Puddles are inevitable in real materials as there are always density fluctuations that locally shift the chemical potential away from the Weyl nodes, while maintaining the overall charge neutrality of the system. In addition, presence of disorder can also support *quasi-localized* rare states at zero-energy even for sub-critical strength of disorder. Although such effects are important and interesting, they do not affect the quantum critical behavior. This is so because rare and critical excitations appear to be decoupled from each other. Also a recent numerical work has demonstrated that such non-perturbative effects can be systematically suppressed with a suitable choice of the distribution of disorder [60]. Therefore, these effects do not alter any physical outcome we reported in this paper.

## Acknowledgments

B. R. was supported by NSF-JQI-PFC and LPS-MPO-CMTC. We thank S. Das Sarma, M. Foster, P. Goswami and S. Bera for useful discussions. B. R. and R. J. S. are thankful to Nordita, Center for Quantum Materials for hospitality during the workshop “From Quantum Field Theories to Numerical Methods” where part of this work was finalized.

## Appendix A: Generalized Harris criterion at WSM-insulator QCP

In this Appendix, we present a generalization of the Harris criterion applicable near the *clean* WSM-insulator QCP. Let us first consider a generalized version of the Hamiltonian from Eq. (6) describing the gapless excita-

tions residing at general WSM-insulator QCP [72]

$$\hat{H}_Q^c(\mathbf{k}, \Delta) = \alpha_c [\sigma_1 k_\perp^c \cos(c\phi_{\mathbf{k}}) + \sigma_2 k_\perp^c \sin(c\phi_{\mathbf{k}})] + \sigma_3 (bk_3^2 - \Delta), \quad (\text{A1})$$

where  $k_\perp = \sqrt{k_x^2 + k_y^2}$  and  $\phi_k = \tan^{-1}(k_y/k_x)$ . The above Hamiltonian for any value of  $\Delta$  possesses the same symmetry, but describes two distinct phases: (i) a band insulator for  $\Delta < 0$  and (ii) WSM for  $\Delta > 0$ , with  $c$  representing the monopole charge of the Weyl nodes. Respectively for  $c = 1, 2$  and  $3$ , single, double and triple WSMs are realized in a crystalline environment [82–84]. The effective dimensionality ( $d_*$ ) of such critical semimetallic phase can be found from the corresponding imaginary time Euclidean action

$$S^c = \int d\tau d^2x_\perp dx_3 \psi^\dagger [\partial_\tau + \hat{H}_Q^c(\mathbf{k} \rightarrow -i\nabla, \Delta)] \psi, \quad (\text{A2})$$

where  $\psi$  is a two component spinor, describing the critical excitations residing at the WSM-insulator QCP. All parameters, such as  $\alpha_c$  and  $b$ , remain invariant under the rescaling of space-time(imaginary) co-ordinates according to  $\tau \rightarrow e^l \tau$ ,  $(x, y) \rightarrow e^{l/c}(x, y)$ ,  $x_3 \rightarrow e^{l/2}x_3$ , when accompanied by the field normalization  $\psi \rightarrow Z_\psi^{1/2}\psi$ , where  $Z_\psi = \exp[-(\frac{2}{c} + \frac{1}{2})l] \equiv \exp[-d_*l]$ . The spatial measure  $d^2x_\perp dx_3 \rightarrow e^{d_*l} d^2x_\perp dx_3$ , where  $d_* = (\frac{2}{c} + \frac{1}{2})$  is the *effective dimensionality* of the system under the rescaling of spatial coordinates. Note that  $\Delta$  in Eq. (A1) is the tuning (relevant) parameter at the WSM-insulator QCP, and the scaling dimension of  $\Delta$ , denoted by  $[\Delta]$ , is tied with the CLE ( $\nu$ ) at this QCP, according to  $\nu^{-1} = [\Delta] = 1$ . Therefore, the stability of the clean WSM-insulator QCP against mass disorder [denoted by  $V_z(\mathbf{x})$  in Eq. (8)] can be assessed from the generalized Harris criterion, suggesting that such QCP is stable against mass disorder when

$$\nu > \frac{2}{d_*} = \frac{4c}{4+c}. \quad (\text{A3})$$

Therefore, only the single ( $c = 1$ ) WSM-insulator QCP is stable against sufficiently weak mass/bond disorder. Furthermore, the stability of the WSM-insulator QCP in the presence of generic disorder, which appears similar to  $V_z(\mathbf{x})$  in Eq. (8), can be established from the generalized Harris criterion (A3). Hence, a single WSM-insulator QCP is guaranteed to be stable against generic disorder. In this regard a comment is due. Our derivation of generalized Harris criterion defers from the original one in Ref. [25], where  $d_*$  is replaced by the physical dimensionality of the system ( $d$ ) and the CLE  $\nu$  varies depending on the nature of the phase transition. On the other hand, within the framework of anisotropic scaling of spatial co-ordinates we always find  $\nu = 1$ , but actual spatial dimension gets replaced by an effective dimensionality of the system ( $d_*$ ) under the process of coarse graining. We believe that these two methods are complimentary to each other.

## Appendix B: RG analysis near WSM-insulator QCP

In this Appendix, we provide technical details of the RG calculations near the WSM-insulator QPT with disorder. First, we show the effects of subleading divergences in the RG flow equations within the  $\epsilon_n$  expansion introduced in Sec. III and its consequences [see Sec. B 1]. Next we display the perturbative analysis of disorder near the WSM-insulator in an expansion about the lower critical dimension of the theory [see Sec B 2].

### 1. $\epsilon_n$ expansion

Within the framework of  $\epsilon_n$  expansion, discussed in Sec. III, when we account for subleading ultraviolet divergences the RG flow equations, , after integrating out the fast Fourier modes within the Wilsonian shell  $\Lambda e^{-l} < k_\perp < \Lambda$  and  $0 < k_3^2 < \infty$ , read

$$\begin{aligned} \beta_X &= X(z - 1 - (\Delta_0 + 2\Delta_\perp + \Delta_z) [h_1(n) + h_2(n)]), \quad \beta_\Delta = \Delta + [\Delta [h_1(n) + h_2(n)] - h_3(n)] (\Delta_0 - 2\Delta_\perp + \Delta_z) \\ \beta_{\Delta_0} &= -\epsilon_n \Delta_0 + 2\Delta_0 (\Delta_0 + 2\Delta_\perp + \Delta_z) [h_1(n) + h_2(n)] + 4\Delta_\perp \Delta_z h_1(n) + 4h_2(n) [\delta_{n,2m} \Delta_0 \Delta_z + \delta_{n,2m+1} \Delta_\perp^2] \\ \beta_{\Delta_\perp} &= -\epsilon_n \Delta_\perp + 2\Delta_\perp (\Delta_z - \Delta_0) h_2(n) + 2\Delta_0 \Delta_3 h_1(n) + 4h_2(n) \Delta_\perp [\delta_{n,2m} \Delta_z + \delta_{n,2m+1} \Delta_0] \\ \beta_{\Delta_z} &= -\epsilon_n \Delta_z + 2\Delta_z (2\Delta_\perp - \Delta_0 - \Delta_z) [h_1(n) - h_2(n)] + 4\Delta_0 \Delta_\perp h_1(n) + 2h_2(n) \delta_{n,2m} (\Delta_0^2 + 2\Delta_\perp^2 + \Delta_z^2), \end{aligned} \quad (\text{B1})$$

where  $\delta_{n,m}$  is the Kronecker delta function,  $n, m$  are integers and  $X = v, b$ . Functions  $h_i(n)$ ,  $i = 1, 2, 3$ , are defined as

$$h_1(n) = \frac{\pi(2n-1) \csc(\frac{\pi}{2n})}{4n^2} = 1 - \frac{1}{2n} + \mathcal{O}(n^{-3})$$

$$\begin{aligned} h_2(n) &= \frac{\pi \csc(\frac{\pi}{2n})}{4n^2} = \frac{1}{2n} + \mathcal{O}(n^{-2}), \\ h_3(n) &= \frac{\pi(n-1) \sec(\frac{\pi}{2n})}{4n^2} = \frac{\pi}{4n} + \mathcal{O}(n^{-2}). \end{aligned} \quad (\text{B2})$$

Therefore, as  $n \rightarrow \infty$  contribution only from  $h_1(n)$  sur-

vives and for any finite  $n$ ,  $h_2(n)$  and  $h_3(n)$  gives rise to *subleading divergences*. The RG flow equations obtained by keeping only the leading divergence are shown in Eq. (10) of the main text. In order to reliably extract the critical exponents, in particular the DSE  $z$  at the multicritical point shown as red dot in Fig. 5, we should only keep the leading order (i.e., as  $n \rightarrow \infty$ ) contribution. At least to the leading order in  $\epsilon_n$  expansion, inclusion of subleading divergences [arising from  $h_2(n)$  and  $h_3(n)$ ] does not alter the value of CLE, and we always find  $\nu^{-1} = \epsilon_n = 1/2$ .

## 2. $\epsilon'_d$ expansion about lower critical dimension

$$d_l = \frac{5}{2}$$

In this section we demonstrate the role of disorder in the vicinity of WSM-insulator QPT perturbatively using an  $\epsilon'_d$  expansion near the lower critical dimension  $d_l = 5/2$  in the theory, where  $\epsilon'_d = d - 5/2$ . As we will see the outcomes are qualitatively the same as in the  $\epsilon_n$  regularization scheme. The exact values of the critical exponents are, however, different from the ones announced in Sec. III, although only slightly so, at least to the one-loop order. Upon integrating the fast modes within the shell  $E_c e^{-l} < \sqrt{v^2 k_\perp^2 + b^2 k_z^4} < E_c$ , where  $E_c$  is the ultraviolet energy cutoff for critical excitations residing the WSM-insulator QCP, we arrive at the following flow equations to the leading order in  $\epsilon'_d$  expansion

$$\begin{aligned} \beta_X &= X [z - 1 - 5(\Delta_0 + 2\Delta_\perp + \Delta_3)], \\ \beta_\Delta &= \Delta + (\Delta - 1)[\Delta_0 - 2\Delta_\perp + \Delta_3], \\ \beta_{\Delta_0} &= -\epsilon'_d \Delta_0 + 10\Delta_0(\Delta_0 + 2\Delta_\perp + \Delta_3) - 16\Delta_3\Delta_\perp, \\ \beta_{\Delta_\perp} &= -\epsilon'_d \Delta_\perp + 2\Delta_\perp(\Delta_3 - \Delta_0) + 4\Delta_3(\Delta_\perp - 2\Delta_0), \\ \beta_{\Delta_3} &= -\epsilon'_d \Delta_3 + 6\Delta_3(2\Delta_\perp - \Delta_0 - \Delta_3) \\ &\quad + 4(\Delta_0^2 + \Delta^2 + \Delta_0\Delta_3 - 4\Delta_0\Delta_\perp + 2\Delta_\perp^2). \end{aligned} \quad (B3)$$

for  $X = v, b$ , after defining the dimensionless disorder coupling constant as  $\Delta_j \alpha \rightarrow \Delta_j$  for  $j = 0, \perp, z$ , where  $\alpha = E_c^{\epsilon'_d} / (20\pi^2 v^2 b^{1/2})$  and  $\Delta/E_c \rightarrow \Delta$ . Therefore, scale independence of  $v$  or  $b$  in the presence of disorder yields a scale dependent dynamic scaling exponent

$$z(l) = 1 + 5[\Delta_0 + 2\Delta_\perp + \Delta_3](l). \quad (B4)$$

The coupled RG flow equations from Eq. (B3) also support only two fixed points: (i)  $(\Delta, \Delta_0, \Delta_\perp, \Delta_3) = (0, 0, 0, 0)$ , representing the WSM-insulator QCP in the clean limit (the blue dot in Fig. 14), and (ii)  $(\Delta, \Delta_0, \Delta_\perp, \Delta_3) = (\frac{0.058}{1+0.058\epsilon'_d} \epsilon'_d, 0.056\epsilon'_d, 0.009\epsilon'_d, 0.02\epsilon'_d)$  representing a multicritical point. The critical exponents at this multicritical point for the anisotropic critical semimetal-metal transition are

$$\nu^{-1} = \epsilon'_d, \quad z = 1 + 0.48\epsilon'_d, \quad (B5)$$

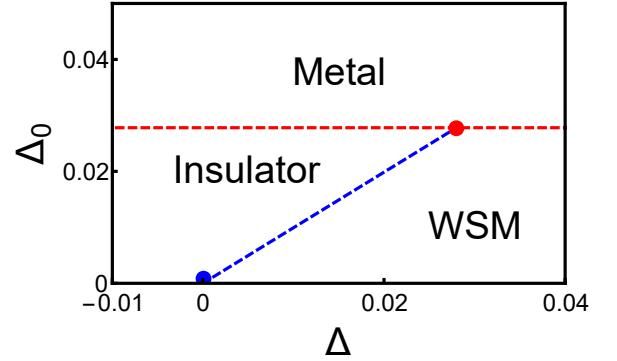


Figure 14: The phase diagram of a dirty Weyl material residing in the close proximity to WSM-insulator QPT, obtained by solving the RG flow equations (B3). Here,  $\Delta$  is the tuning parameter for WSM-insulator transition in the clean system and  $\Delta_0$  is the strength of random charge impurities.

which is extremely close to the ones reported in Sec. III for  $\epsilon'_d = 1/2$ . Therefore, both methods produce qualitatively similar results near WSM-insulator QPT, and the obtained critical exponents for anisotropic semimetal-metal transition are extremely close to each other, at least to the leading order. The resulting phase diagram is shown in Fig. 14.

## Appendix C: Details of $\epsilon_m$ expansion

In this appendix we display the detailed analysis of various one-loop diagrams, shown in Fig. 6, within the framework of an  $\epsilon_m$  expansion.

### 1. Self-energy

Let us first consider the self energy diagram in Fig. 6(a). The expression for the self-energy reads

$$\begin{aligned} \Sigma(i\omega, \mathbf{k}) &= \sum_N \int \frac{d^d \mathbf{q}}{(2\pi)^d} N G_0(i\omega, \mathbf{k} - \mathbf{q}) N \frac{\Delta_N}{q^m} \\ &\equiv \sum_N \Sigma_N(i\omega, \mathbf{k}), \end{aligned} \quad (C1)$$

with  $d = 3$ , the summation is taken over all eight types of disorder (see Table II) and  $q \equiv |\mathbf{q}|$ .

The contribution from one-loop self-energy diagram from the disorder represented by the matrix  $N$  reads

$$\Sigma_N(i\omega, \mathbf{k}) = -i\Delta_N \int \frac{d^3 \mathbf{q}}{(2\pi)^3} \frac{N [\gamma_0 \omega + v \gamma_j (k - q)_j] N}{[\omega^2 + v^2 (\mathbf{k} - \mathbf{q})^2] q^m}. \quad (C2)$$

We will evaluate the temporal and spatial components of the self-energy diagram separately. Let us first set  $\mathbf{k} = 0$ ,

for which

$$\begin{aligned}\Sigma_N(i\omega, 0) &= \Delta_N(-i\omega) \frac{N\gamma_0 N}{v^{3-m}} \int \frac{d^3\mathbf{q}}{(2\pi)^3} \frac{1}{(\omega^2 + q^2)q^m} \\ &= \Delta_N(-i\omega) \frac{N\gamma_0 N}{v^{3-m}} \frac{\Gamma(1 + \frac{m}{2})}{\Gamma(m/2)} \\ &\times \int_0^1 dx x^{\frac{m}{2}-1} \int \frac{d^3\mathbf{q}}{(2\pi)^3} \frac{1}{[q^2 + (1-x)\omega^2]^{1+\frac{m}{2}}},\end{aligned}\quad (\text{C3})$$

where  $x$  is the Feynman parameter. Upon completing the integrals over  $q$  and  $x$ , and setting  $m = 1 - \epsilon$  (for brevity, we use here shorthand notation  $\epsilon_m \rightarrow \epsilon$ ) we obtain

$$\Sigma_N(i\omega, 0) = [iN\gamma_0\omega N] \left( \frac{\Delta_N}{2\pi^2 v^2} \right) \frac{1}{\epsilon} + \mathcal{O}(1). \quad (\text{C4})$$

Next we set  $\omega = 0$  and the spatial component of self-energy correction is then given by

$$\begin{aligned}\Sigma_N(0, \mathbf{k}) &= \Delta_N [-iN\gamma_j N] \frac{1}{v^{3-m}} \int \frac{d^3\mathbf{q}}{(2\pi)^3} \frac{(k-q)_j}{(\mathbf{k}-\mathbf{q})^2 q^m} \\ &= \Delta_N \left( \frac{-iN\gamma_j N}{v^{3-m}} \right) \frac{\Gamma(1 + \frac{m}{2})}{\Gamma(m/2)} \int_0^1 dx x^{\frac{m}{2}-1} \\ &\times \int \frac{d^3\mathbf{q}}{(2\pi)^3} \frac{(k-q)_j}{[q^2 - 2(1-x)\mathbf{q} \cdot \mathbf{k} + (1-x)k^2]^{1+\frac{m}{2}}}. \quad (\text{C5})\end{aligned}$$

After shifting the momentum variable according to  $\mathbf{q} - (1-x)\mathbf{k} \rightarrow \mathbf{q}$  and setting  $m = 1 - \epsilon$ , we obtain

$$\Sigma_N(0, \mathbf{k}) = [iN\gamma_j k_j N] \left( \frac{\Delta_N}{2\pi^2 v^2} \right) \frac{1}{3\epsilon} + \mathcal{O}(1). \quad (\text{C6})$$

Hence, the total self energy correction reads

$$\Sigma_N(i\omega, \mathbf{k}) = iN \left[ \gamma_0\omega + \frac{1}{3}\gamma_j k_j \right] N \Delta_N \frac{1}{\epsilon} + \mathcal{O}(1), \quad (\text{C7})$$

where we have redefined  $\Delta_N/(2\pi^2 v^2) \rightarrow \Delta_N$ , which is Eq. (20) in the main text.

## 2. Vertex

The vertex correction for the disorder vertex shown in Fig. 6(b) with the matrix  $N$  reads

$$V_N(\mathbf{k}) = \sum_M \int \frac{d^3\mathbf{q}}{(2\pi)^3} M G_0(0, \mathbf{k}-\mathbf{q}) N G_0(0, \mathbf{k}-\mathbf{q}) M \frac{\Delta_M}{q^m}, \quad (\text{C8})$$

where we kept only one external momentum as an infrared regulator. The last expression can be compactly written as

$$V_N(\mathbf{k}) = - \sum_M [M\gamma_j N\gamma_l M] \frac{\Delta_M}{v^2} I_{jl}(\mathbf{k}), \quad (\text{C9})$$

where

$$I_{jl}(\mathbf{k}) = \int \frac{d^3\mathbf{q}}{(2\pi)^3} \frac{(k-q)_j(k-q)_l}{(\mathbf{q}-\mathbf{k})^4 q^m}. \quad (\text{C10})$$

We now present the evaluation of the above integral

$$\begin{aligned}I_{jl} &= \int \frac{d^3\mathbf{q}}{(2\pi)^3} \frac{(k-q)_j(k-q)_l}{(\mathbf{k}-\mathbf{q})^4 q^m} \\ &= \frac{\Gamma(2 + \frac{m}{2})}{\Gamma(m/2)} \int_0^1 dx x(1-x)^{\frac{m}{2}-1} \\ &\times \int \frac{d^3\mathbf{q}}{(2\pi)^3} \frac{(k-q)_j(k-q)_l}{[x(\mathbf{k}-\mathbf{q})^2 + (1-x)q^2]^{2+\frac{m}{2}}}. \quad (\text{C11})\end{aligned}$$

After shifting the momentum variable as  $\mathbf{q} - x\mathbf{k} \rightarrow \mathbf{q}$ , we obtain

$$\begin{aligned}I_{jl} &= \frac{\Gamma(2 + \frac{m}{2})}{\Gamma(m/2)} \int_0^1 dx x(1-x)^{\frac{m}{2}-1} \\ &\times \int \frac{d^3\mathbf{q}}{(2\pi)^3} \frac{(q - (1-x)k)_j(q - (1-x)k)_l}{[q^2 + x(1-x)k^2]^{2+\frac{m}{2}}} \\ &= -\frac{k^{-\epsilon}}{2\pi^2} \frac{\delta_{jl}}{3\epsilon} + \mathcal{O}(1), \quad (\text{C12})\end{aligned}$$

after taking  $m = 1 - \epsilon$ , since only the  $q$ -dependent part in the numerator of the integrand yields a divergent contribution. We use the last expression to obtain Eq. (27) in the main text.

## Appendix D: Lattice realization of generic disorder in Weyl semimetal

In this appendix, we demonstrate the lattice realization of *sixteen* possible fermionic bilinears (shown in Table II) from the two band tight-binding model, displayed in Eqs. (5) and (3). By the virtue of the chosen tight-binding model, our construction is based on two features:

- Since two Weyl nodes are located on the  $k_z$  axis at  $\pm k_z^0 = \pm\pi/(2a)$ , any fermionic bilinear *odd* under the exchange of two Weyl nodes, can be realized by adding  $h = \sum_{\mathbf{k}} \Psi_{\mathbf{k}}^{\dagger} \sin(k_z a) \sigma_j \Psi_{\mathbf{k}}$  to the tight binding model, where  $j = 0, 1, 2, 3$ . Such perturbation corresponds to an imaginary hopping along the  $z$  direction, and does not renormalize the band width.
- Any fermionic bilinear that couples two Weyl nodes, which therefore necessarily breaks translational symmetry, can be realized through a periodic and *commensurate* modulation of the nearest-neighbor hopping amplitude, but only along the  $z$  direction.

With these two construction principles we can realize all sixteen fermion bilinears by adding the following terms to the tight-binding Hamiltonian.

### 1. Regular chemical potential:

$$\sum_{\mathbf{r}} \Psi_{\mathbf{r}}^{\dagger} V(\mathbf{r}) \sigma_0 \Psi_{\mathbf{r}},$$

2. Axial chemical potential:

$$\sum_{\mathbf{r}} \Psi_{\mathbf{r}}^{\dagger} \left[ \frac{iV(\mathbf{r})}{2} \sigma_0 \right] \Psi_{\mathbf{r}+\hat{e}_3} + H.c.,$$

3. Abelian current:

$$\sum_{\mathbf{r}} \left[ \Psi_{\mathbf{r}}^{\dagger} \left[ \frac{iV(\mathbf{r})}{2} \sigma_3 \right] \Psi_{\mathbf{r}+\hat{e}_3} + H.c. + \Psi_{\mathbf{r}}^{\dagger} V(\mathbf{r}) (\sigma_1 + \sigma_2) \Psi_{\mathbf{r}} \right],$$

4. Abelian axial-current:

$$\sum_{\mathbf{r}} \left[ \Psi_{\mathbf{r}}^{\dagger} \left[ \frac{iV(\mathbf{r})}{2} (\sigma_1 + \sigma_2) \right] \Psi_{\mathbf{r}+\hat{e}_3} + H.c. + \Psi_{\mathbf{r}}^{\dagger} V(\mathbf{r}) \sigma_3 \Psi_{\mathbf{r}} \right],$$

5. Temporal components of tensor:

$$\sum_{\mathbf{r}} \sum_j (-1)^j \Psi_{\mathbf{r},j}^{\dagger} V(r) [\sigma_1 + \sigma_2 + i\sigma_0] \Psi_{\mathbf{r},\hat{e}_3,j+1} + H.c.,$$

6. Spatial components of tensor:

$$\sum_{\mathbf{r}} \sum_j (-1)^j \Psi_{\mathbf{r},j}^{\dagger} V(r) [\sigma_0 + i\sigma_1 + i\sigma_2] \Psi_{\mathbf{r},\hat{e}_3,j+1} + H.c.$$

7. Scalar mass:

$$\sum_{\mathbf{r}} \sum_j (-1)^j \Psi_{\mathbf{r},j}^{\dagger} [V(r) \sigma_3] \Psi_{\mathbf{r},\hat{e}_3,j+1} + H.c.,$$

8. Pseudo-scalar mass:

$$\sum_{\mathbf{r}} \sum_j (-1)^j \Psi_{\mathbf{r},j}^{\dagger} [iV(r) \sigma_3] \Psi_{\mathbf{r},\hat{e}_3,j+1} + H.c.$$

Thus, within the simplest realization of a Weyl semimetal from a tight-binding model on a cubic lattice, one can realize all possible disorder couplings by choosing  $V(\mathbf{r})$  as a random variable, and numerically study possible WSM-metal QPTs.

- 
- [1] C. Herring, Phys. Rev. **52**, 365 (1937).  
[2] R. Dornhaus, G. Nimtz, and B. Schlicht, *Narrow-Gap Semiconductors*, (Springer-Verlag, 1983).  
[3] G. E. Volovik, *The Universe in a Helium Droplet* (Oxford University Press, New York, 2003).  
[4] T. O. Wehling, A. M. Black-Schaffer, A. V. Balatsky, Adv. Phys. **76**, 1 (2014), and references therein.  
[5] C.-K. Chiu, J. C. Y. Teo, A. P. Schnyder, and S. Ryu, Rev. Mod. Phys. **88**, 035005 (2016), and references therein.  
[6] A. Bansil, Hsin Lin, and Tanmoy Das, Rev. Mod. Phys. **88**, 021004 (2016), and references therein.  
[7] B. Bradlyn, J. Cano, Z. Wang, M.G. Vergniory, C. Felser, R. J. Cava, B. A. Bernevig, arXiv:1603.03093  
[8] B. J. Wieder and C. L. Kane, Phys. Rev. B **94**, 155108 (2016).  
[9] R-J. Slager, V. Juricic, V. Lahtinen, J. Zaanen, Phys. Rev. B **93**, 245406 (2016).  
[10] A. A. Burkov, J. Phys.: Condens. Matter. **27**, 113201 (2015).  
[11] S. Rao, arXiv:1603.02821 (2016).  
[12] P. A. M. Dirac, Proc. Roy. Soc. A **117**, 610 (1928); *ibid.* **126**, 360 (1930).  
[13] H. Weyl, Z. Physik **56**, 330 (1929).  
[14] C. Zhang, Z. Yuan, S. Xu, Z. Lin, B. Tong, M. Z. Hasan, J. Wang, C. Zhang, S. Jia, arXiv:1502.00251  
[15] S-Y. Xu, I. Belopolski, N. Alidoust, M. Neupane, C. Zhang, R. Sankar, S-M. Huang, C-C. Lee, G. Chang, B. Wang, G. Bian, H. Zheng, D. S. Sanchez, F. Chou, H. Lin, S. Jia, M. Z. Hasan, Science **349**, 613 (2015).  
[16] B. Q. Lv, H. M. Weng, B. B. Fu, X. P. Wang, H. Miao, J. Ma, P. Richard, X. C. Huang, L. X. Zhao, G. F. Chen, Z. Fang, X. Dai, T. Qian, H. Ding, Phys. Rev. X **5**, 031013 (2015)  
[17] S-Y. Xu, N. Alidoust, I. Belopolski, C. Zhang, G. Bian, T-R. Chang, H. Zheng, V. Strokov, D. S. Sanchez, G. Chang, Z. Yuan, D. Mou, Y. Wu, L. Huang, C-C. Lee, S-M. Huang, B. Wang, A. Bansil, H-T. Jeng, T. Neupert, A. Kaminski, H. Lin, S. Jia, M. Z. Hasan, Nature Physics **11**, 748 (2015).  
[18] N. Xu, H. M. Weng, B. Q. Lv, C. Matt, J. Park, F. Bisti, V. N. Strokov, D. gawryluk, E. Pomjakushina, K. Conder, N. C. Plumb, M. Radovic, G. Autès, O. V. Yazayev, Z. Fang, X. Dai, G. Aeppli, T. Qian, J. Mesot, H. Ding, M. Shi, arXiv:1507.03983  
[19] C. Shekhar, A. K. Nayak, Y. Sun, M. Schmidt, M. Nicklas, I. Leermakers, U. Zeitler, Z. Liu, Y. Chen, W. Schnelle, J. Grin, C. Felser, B. Yan, arXiv:1502.04361  
[20] Z. Wang, Y. Zheng, Z. Shen, Y. Zhou, X. Yang, Y. Li, C. Feng, Z-A. Xu, arXiv:1506.00924  
[21] G. Chang, S-Y. Xu, D. S. Sanchez, S-M. Huang, C-C. Lee, T-R. Chang, H. Zheng, G. Bian, I. Belopolski, N. Alidoust, H-T. Jeng, A. Bansil, H. Lin, M. Z. Hasan, arXiv:1512.08781  
[22] S. Borisenko, D. Evtushinsky, Q. Gibson, A. Yaresko, T. Kim, M. N. Ali, B. Buechner, M. Hoesch, R. J. Cava, arXiv:1507.04847  
[23] J. Y. Liu, J. Hu, Q. Zhang, D. Graf, H. B. Cao, S. M. A. Radmanesh, D. J. Adams, Y. L. Zhu, G. F. Cheng, X. Liu, W. A. Phelan, J. Wei, D. A. Tennant, J. F. DiTusa, I. Chiorescu, L. Spinu, Z.Q. Mao, arXiv:1507.07978.  
[24] H.B. Nielsen, and M. Ninomiya, Nucl. Phys. B **185**, 20 (1981); Phys. Lett. B **105**, 219 (1981).  
[25] A. B. Harris, J. Phys. C **7**, 1671 (1974).

- [26] E. Fradkin, Phys. Rev. B **33**, 3263 (1985).
- [27] R. Shindou, and S. Murakami, Phys. Rev. B **79**, 045321 (2009).
- [28] P. Goswami, and S. Chakravarty, Phys. Rev. Lett. **107**, 196803 (2011).
- [29] S. Ryu and K. Nomura, Phys. Rev. B **85**, 155138 (2012).
- [30] P. Hosur, S. A. Parameswaran, A. Vishwanath, Phys. Rev. Lett. **108**, 046602 (2012).
- [31] Z. Huang, T. Das, A. V. Balatsky, and D. P. Arovas, Phys. Rev. B **87**, 155123 (2013).
- [32] R. Nandkishore, D. A. Huse, S. L. Sondhi, Phys. Rev. B **89**, 245110 (2014).
- [33] Y. Ominato, and M. Koshino, Phys. Rev. B **89**, 054202 (2014); Phys. Rev. B **91**, 035202 (2015).
- [34] B. Roy, and S. Das Sarma, Phys. Rev. B **90**, 241112(R) (2014).
- [35] S. V. Syzranov, L. Radzihovsky, V. Gurarie, Phys. Rev. Lett. **114**, 166601 (2015); S. V. Syzranov, V. Gurarie, L. Radzihovsky, Phys. Rev. B **91**, 035133 (2015).
- [36] E-G. Moon, Y-B. Kim, arXiv:1409.0573
- [37] A. Altland, and D. Bagrets, Phys. Rev. Lett. **114**, 257201 (2015).
- [38] B. Roy, S. Das Sarma, Phys. Rev. B **93**, 119911 (E) (2016).
- [39] B. Roy, S. Das Sarma, Phys. Rev. B **94**, 115137 (2016).
- [40] B. Roy, V. Jurićć, S. Das Sarma, Sci. Rep. **6**, 32446 (2016).
- [41] P. Goswami, and S. Chakravarty, arXiv:1603.03763
- [42] T. Louvet, D. Carpentier, A. A. Fedorenko, arXiv:1605.02009
- [43] S. V. Syzranov, V. Gurarie, L. Radzihovsky, arXiv:1604.07947
- [44] A. K. Mitchell, and L. Fritz, Phys. Rev. B **93**, 035137 (2016).
- [45] E. V. Gorbar, V. A. Miransky, I. A. Shovkovy, and P. O. Sukhachov, Phys. Rev. B **93**, 235127 (2016).
- [46] M. J. Park, B. Basa, M. J. Gilbert, arXiv:1608.06311
- [47] T. Louvet, D. Carpentier, A. A. Fedorenko, arXiv:1609.08368
- [48] K. Kobayashi, T. Ohtsuki, K-I. Imura, Phys. Rev. Lett. **110**, 236803 (2013).
- [49] K. Kobayashi, T. Ohtsuki, K-I. Imura, I. F. Herbut, Phys. Rev. Lett. **112**, 016402 (2014).
- [50] B. Sbierski, G. Pohl, E. J. Bergholtz, P. W. Brouwer, Phys. Rev. Lett. **113**, 026602 (2014).
- [51] J. H. Pixley, P. Goswami, and S. Das Sarma, Phys. Rev. Lett. **115**, 076601 (2015).
- [52] B. Sbierski, E. J. Bergholtz, P. W. Brouwer, Phys. Rev. B **92**, 115145 (2015).
- [53] J. H. Pixley, P. Goswami, and S. Das Sarma, Phys. Rev. B **93**, 085103 (2016).
- [54] S. Liu, T. Ohtsuki, R. Shindou, Phys. Rev. Lett. **116**, 066401 (2016).
- [55] C-Z. Chen, J. Song, H. Jiang, Q-F Sun, Z. Wang, X. C. Xie, Phys. Rev. Lett. **115**, 246603 (2015).
- [56] S. Bera, J. D. Sau, and B. Roy, Phys. Rev. B **93**, 201302 (2016).
- [57] H. Shapourian, T. L. Hughes, Phys. Rev. B **93**, 075108 (2016).
- [58] J. H. Pixley, D. A. Huse, S. Das Sarma, Phys. Rev. X **6**, 021042 (2016).
- [59] B. Roy, Y. Alavirad, J. D. Sau, arXiv:1604.01390
- [60] J. H. Pixley, D. A. Huse, S. Das Sarma, Phys. Rev. B **94**, 121107 (R) (2016).
- [61] Y. Takane, arXiv:1609.07822.
- [62] B. Roy, and J. D. Sau, Phys. Rev. B **92**, 125141 (2015).
- [63] We assume here that magnetic impurities are dilute, so that we do not have to worry about Kondo effect.
- [64] C.-X. Liu, X.-L. Qi, H.-J. Zhang, X. Dai, Z. Fang, and S-C. Zhang, Phys. Rev. B **82**, 045122 (2010).
- [65] C-X. Liu, P. Ye, X-L. Qi, Phys. Rev. B **87**, 235306 (2013).
- [66] P. Goswami, and B. Roy, arXiv:1211.4023, and references therein.
- [67] X. Li and B. Roy, arXiv:1608.06632.
- [68] A. Weiße, G. Wellein, A. Alverman, and H. Feshke, Rev. Mod. Phys. **78**, 275 (2006).
- [69] For comprehensive discussion on Anderson transition see *50 Years of Anderson Localization*, edited by E. Abrahams (World Scientific Publishing Company, 1st ed., 2010).
- [70] R-J. Slager, A. Mesaros, V. Juricic, J. Zaanen, Nature Physics **9**, 98 (2013).
- [71] J. Zinn-Justin, *Quantum Field Theory and Critical Phenomena* (Oxford University Press, Oxford, UK, 2002).
- [72] B. Roy, P. Goswami, and V. Jurićć, arXiv:1610.05762
- [73] See A. Weinrib and B. I. Halperin, Phys. Rev. B **27**, 413 (1983) for general discussion on correlated disorder.
- [74] S. Sachdev, *Quantum Phase Transitions* (Cambridge University Press, 2nd ed., 2007).
- [75] I. F. Herbut, V. Jurićć, B. Roy, Phys. Rev. B **79**, 085116 (2009).
- [76] Y. Otsuka, S. Yunoki, S. Sorella, Phys. Rev. X **6**, 011029 (2016).
- [77] F. Wegner, Z. Phys. B **25**, 327 (1976).
- [78] S. Borisenko, Q. Gibson, D. Evtushinsky, V. Zabolotnyy, B. Buechner, and R. J. Cava, Phys. Rev. Lett. **113**, 027603 (2014).
- [79] Z. K. Liu, B. Zhou, Y. Zhang, Z. J. Wang, H. M. Weng, D. Prabhakaran, S.-K. Mo, Z. X. Shen, Z. Fang, X. Dai, Z. Hussain, Y. L. Chen, Science **343**, 864 (2014).
- [80] S. Das Sarma, S. Adam, E. H. Hwang, and E. Rossi, Rev. Mod. Phys. **83**, 407 (2011).
- [81] B. I. Halperin, and M. Lax, Phys. Rev. **148**, 722 (1966).
- [82] G. Xu, H. Weng, Z. Wang, X. Dai, and Z. Fang, Phys. Rev. Lett. **107**, 186806 (2011).
- [83] C. Fang, M. J. Gilbert, X. Dai, and B. A. Bernevig, Phys. Rev. Lett. **108**, 266802 (2012).
- [84] B-J. Yang, and N. Nagaosa, Nat. Commun. **5**, 4898 (2014).